Dipartimento di Fisica

CORSO DI LAUREA IN FISICA

TESI DI LAUREA

Simulation studies of the dual radiator RICH of the ePIC experiment at EIC

Laureando:
Tiziano Boasso

Relatrice:
Dott.ssa Silvia Dalla Torre

Correlatore:
Dr. Chandradoy Chatterjee

ANNO ACCADEMICO 2022-2023

Summary

The goals of this thesis are original simulation studies contributing to the design of the dual radiator Ring Imaging CHerenkov counter (dRICH) of the ePIC experiment at the Electron-Ion Collider (EIC). The context of these studies is provided in Chapter 1, where an introduction to the physics scope of the EIC and the ePIC experiment is provided, Chapter 2, which introduces the EIC project and the ePIC experiment, in Chapter 3, where basic concepts about particle identification by Cherenkov techniques are recalled and Chapter 4, which describes the overall particle identification system of the ePIC experiment.

The original studies, performed by the student author of this thesis, are reported in Chapter 5. Three issues relevant for the dRICH design have been addressed, two of them related to the novelty of the selected sensors of single photons, namely Silicon PhotoMultipliers (SiPM), this being the first time they are used in a Cherenkov imaging detector:

- The dependence of the dRICH performance versus the parameters of one of the two radiators, the aerogel, in view of optimizing the choice of the parameters to be fixed for this radiator.
- The distributions of the angles of the Cherenkov photon trajectories respect to the photosensor surface; this information is relevant as, when the trajectory is far from the orthogonal direction, the optical properties of the entrance window of the photosensor can reduce the number of detected photons.
- A feature of the selected photosensors is the relevant dark count rate, where the dark signals are non distinguishable from the single photon signals. The presence of this background affects the dRICH performance. The studies presented in this thesis are the first estimation of the dRICH performance degradation caused by the dark counts.

The impact of the studies performed within this thesis is underlined in Chapter 6.

Table of Contents

Chapter 1

Mystery of Protons: Path to QCD

1.1 Historical Introduction

The path to Quantum ChromoDynamics (QCD) is via the deeper and deeper exploration of the protons and, later, of the other particles that experience the same dynamics.

Dirac's theory on electron predicted that the magnetic moment is related to the Bohr magneton (μ_B) with a dimensionless constant (g) known as *g-factor* of value 2. This is due to the elementary particle nature of the electron and the quantum nature of its spin. Dirac in 1930 posited that like electrons also protons are point like particles. Their magnetic dipole moments, namely, Bohr magneton (μ_B) and nuclear magneton (μ_N) are related to the ratio of their masses. By deflecting the molecular hydrogen in presence of magnetic field, Otto Stern and Immanuel Estermann concluded that the proton's dipole moment (μ_P) is not that of a Dirac's elementary particle, rather $\mu_P \sim$2-3μ_M [**estermann1933magnetic**]. The most recent measurements suggest that this anomalous magnetic moment is $\mu_P \sim 2.79\mu_M$. The electron however, followed the predictions of Dirac and cosmic ray studies confirmed the existence of positron, the anti-particle of electron. In 1932 Chadwick discovered the neutron, the uncharged sister particle of the proton, residing inside the atomic nucleus. A key question remained open: how the positively charged protons can cohabit inside a dense nucleus. In the 1950s, the experiment by Segre, Chamberlin et al. demonstrated the existence of antiproton, despite not being a Dirac particle.

Progress in understanding the proton puzzle came from the electron-proton scattering studies accompanied by quantum field theory, which provided an insight to the mechanism behind the lepton scattering: the scattered lepton exchanges a

virtual photon. This photon is virtual in the sense that the photons do not precisely obey the Energy-momentum relation and hence they are in the off-mass shell state. Nevertheless, the transferred 4-momentum of the lepton is the 4-momentum of the photon (the leptons are real particle), and gives us the scale of resolution to the length scale we are probing. The transferred 4-momentum squared is denoted by q^2. For convention $Q^2 = -q^2$ are used. The energy of the virtual photon (ν) is the difference between the energy of the incoming (E_1) and scattered (E_2) lepton.

In the fifties of the twentieth century, a rapid decrease in the cross-section when probing the proton with high-energy electrons was measured, interpreted as due to the finite size of the proton. For a finite size charge distribution the point like scattering cross-section has been modified with the introduction of two form factors F_1 and F_2, a linear combination of F_1 and F_2 leads to the so-called electric and magnetic form factors of the proton G_E and G_M, which are taken into account for a single photon exchange in the so-called Rosenbluth formulation.

In the 1950s and 60s a set of new particles was discovered, globally referred to as hadrons. M. Gell-Mann and Y. Neeman showed that these particles can be grouped in octets (mesons and baryons) or decuplets (hyperons) as a representation of a SU(3) symmetry group. Nevertheless, it was hard to believe that all of them were elementary particles and that the simplest representation of this group, namely a triplet, was not realised in nature.
Therefore, to describe the "particle zoo" of hadrons in terms of SU(3) representations, Gell-Mann and Zweig [**gell2010schematic**, **narison2004qcd**] proposed that hadrons result from entities with spin$\frac{1}{2}$, point-like charged particles, that Gell-Mann called quarks. In this scheme, mesons are bound quark anti-quark systems and baryons are bound three quark systems. This assumption implied attributing peculiar features to the constituent quarks. Their charges are fractional and they would violate the spin-statistics of spin$\frac{1}{2}$ particles. The violation was overcome by postulating a new further quantum number, also associated to an SU(3) symmetry: the color [**pich1995quantum**].

In the sixties, the seminal SLAC-MIT collaboration made a series of Deep Inelastic Scattering (DIS) experiments, thanks to the increased electron beam energy of 20 GeV, it was a first of a kind [**breidenbach1969observed**]. It was observed that the eletron-proton cross-section instead of rapidly decreasing with Q^2 was measured to scale to the probing energy. In other words, the electrons scattered at large angles were observed scaled with Q^2, indicating that protons indeed have internal structures. Feynman called the substructure elements partons [**feynman1969very**]. The debate about the identification of partons as quarks passionated the following year and, nowadays, it is universally accepted.

In 1969, Bjorken demonstrated that in the limit the interaction energy is much larger than the mass of the proton ("infinte momentum frame"), the form factor F_2 introduced to describe the DIS scattering cross-section,should scale with the

function of the fractional momentum of the parent proton is carried by the partons, called in other words, Bjorken-x (denoted as x_B); in other words, F_2 is not depending on the Q^2. This is known as the Bjorken scaling.

In parallel, the QCD was proposed as the theory of the nuclear or strong force responsible of the stability of the nuclei. The theory was further developed introducing, near the quarks, the force mediators, called gluons. Gluons, eight of them and carrying colour charge, play for QCD a role similar to that of the photons for quantum electrodynamics. QCD has peculiar features. Quarks are never seen as a free particle in nature and no observed hadron has color charge different from zero. The asymptotic freedom of quark namely the interaction becaming weaker as the energy scale increases and the corresponding length scale decreases, is a feature coming out from the nature of the strong interaction as predicted by QCD. It was demonstarted that, at sufficiently smaller length scale (higher energies), the interaction becomes weak and the quarks behave as free particle and the interaction can be perturbatively expanded. However, with increasing length scale (lower energy scale) the interaction becomes stronger. This behavior is exactly opposite to that of the electromagnetic interaction. Also the running of the coupling constant of the strong interaction (α_s) became an experimental evidence [**close1993consistent**].

QCD opened the way to explain the non zero magnetic moment of neutrons and the existence of numerous protons inside the nucleus. The existence of different colors of the quarks became more evident measuring the ratio of the cross-sections of muon production and hadron production in electron-positron collider experiments at different centre of mass energy. Nevertheless, more open questions arised. The EMC Experiment in the 80s at CERN, using as lepton probes the muons from a secondary SPS beam, provided indications for new puzzles: the evidence that the cross section for DIS from an atomic nucleus is different from that of the same number of free protons and neutrons, the so called "EMC effect", and that the quarks do not provide the dominant contribution of the spin of the proton, generating the "spin crisis".

Aided with high centre of mass energy collision and analyzing data collected in different experiment like EMC(CERN) BCDMS(CERN), NMC(CERN), H1(DESY), Zeus(DESY) and E666(FermiLab), it was demonstrated that the scaling of the structure function violates with very large or small value of x_B is violated. The data had been described with the so-called DGLAP equation, where it had been understood that with very high Q^2, deep inelastic scattering is sensitive to cases when a quark radiates gluons and hence carries only a very small fraction of the protons momentum. This is consistent with QCD prediction.

It became also evident that the quarks have a nonzero transverse momentum, a contribution initially ignored. Experiments like HERMES, COMPASS and CLAS (JLAB) explored the transverse world inside the nucleons. These evidences require

highly polarized nucleons and lepton scattering.

Despite a lot of progress in the understanding of the internal structure of the proton, the role-play of the dynamics of the quarks and the gluons to the macroscopic properties of the protons or nuclei are still not complete. New experimental data with high statistics coming from collisions of the lepton and ion with high degree of polarization is necessary. The Electron Ion Collider (EIC) aims to be the ultimate facility to explore the internal structure of the nucleons and emerging properties of nuclei that has never been explored before (Sec. 1.2).

1.2 The Electron Ion collider physics scope

The Electron Ion Collider (EIC) is going to address some of the most fundamental open questions related to QCD and hadronic matter[**accardi2014electron**]. It will primarily address these following domains of investigation:

- how do the nucleonic properties such as mass and spin emerge from partons and their underlying interactions?
- How are partons inside the nucleon distributed in both momentum and position space?
- How do color-charged quarks and gluons, and jets, interact with a nuclear medium? How do the confined hadronic states emerge from these quarks and gluons? How do the quark-gluon interactions create nuclear binding?
- How does a dense nuclear environment affect the dynamics of quarks and gluons, their correlations, and their interactions? What happens to the gluon density in nuclei? Does it saturate at high energy, giving rise to gluonic matter or a gluonic phase with universal properties in all nuclei and even in nucleons?

Clearly, to achieve these physics benchmarks, the EIC has to navigate a kinematic phase-space wider than that has been explored so far and offer largely improved precision thanks to high luminosity (Sec. 2.1). These features allow to have important overlap with the past experiments and pave the way into unexplored phase-space of QCD (Fig. 1.1), making possible the extraction of information in the low-x region thanks to the energy domain and, therefore, providing critical information about the gluon-dominated regime, and the high-x region thanks to the high luminosity.

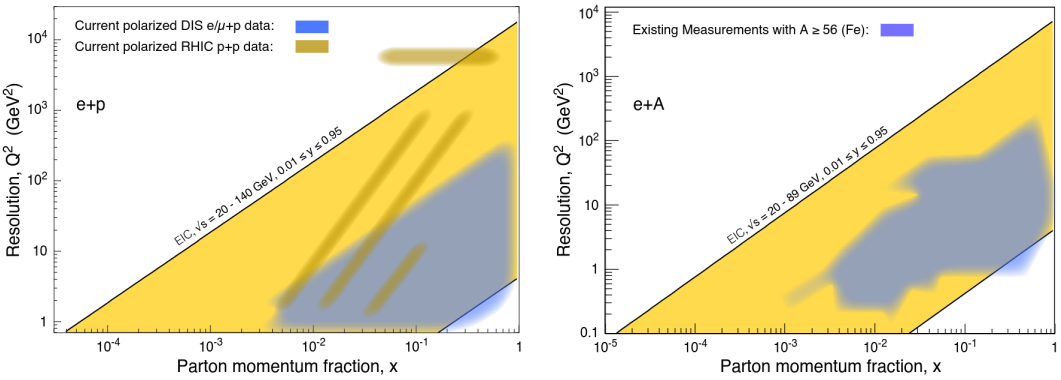

Figure 1.1: x-Q^2 kinematics covered by EIC (Yellow) of e+p (left hand plot) and e+A collision (right hand plot). The blue region demonstrates the coverage of existing measurements from lepton nucleon scattering at CERN, DESY, JLab and SLAC along with polarized p+p scattering at RHIC.

Chapter 2

The Electron Ion Collider and the ePIC experiment

2.1 The Electron Ion Collider Project

The EIC is an approved project in the USA [**NAP25171**]. The project includes the collider and the ePIC experiment (Sec. 2.2).

The collider is a complex of particle accelerators with unprecedented parameters: luminosity up to 10^{34} $s^{-1}cm^{-2}$ in e-p scattering, a variable centre of mass energy ($\sqrt{s}$) between 21-141 GeV/c^2, highly polarized e+p scattering (70% polarization) and e+A scattering with a large variety of ions from H to U. A schematic overview of the EIC Collider is provided in Fig. 2.1.

The project was approved in 2019, the current phase is that of the collider and detector design, the start of the construction phase is expected in 2025 and its completion is scheduled in the first years of the 2030s. It will take place at the Brookhaven National Laboratory (BNL), Upton New-York U.S.A, where the RHIC collider is set. RHIC is an ion-ion collider, and as such it provides most of the civil engineering needed for the EIC, like the tunnel and the ion acceleration and storage ring, and even the whole complex of the proton polarized sources and the acceleration chain compatible with polarized ions. The electron complex, including the polarized source, the acceleration chain and the storage ring are new and they will be construct in the next years. The collider lattice allows for two interaction points: one of them will host the ePIC detector, included in the EIC project, that will be discuss in the next section, the second one can be instrumented later.

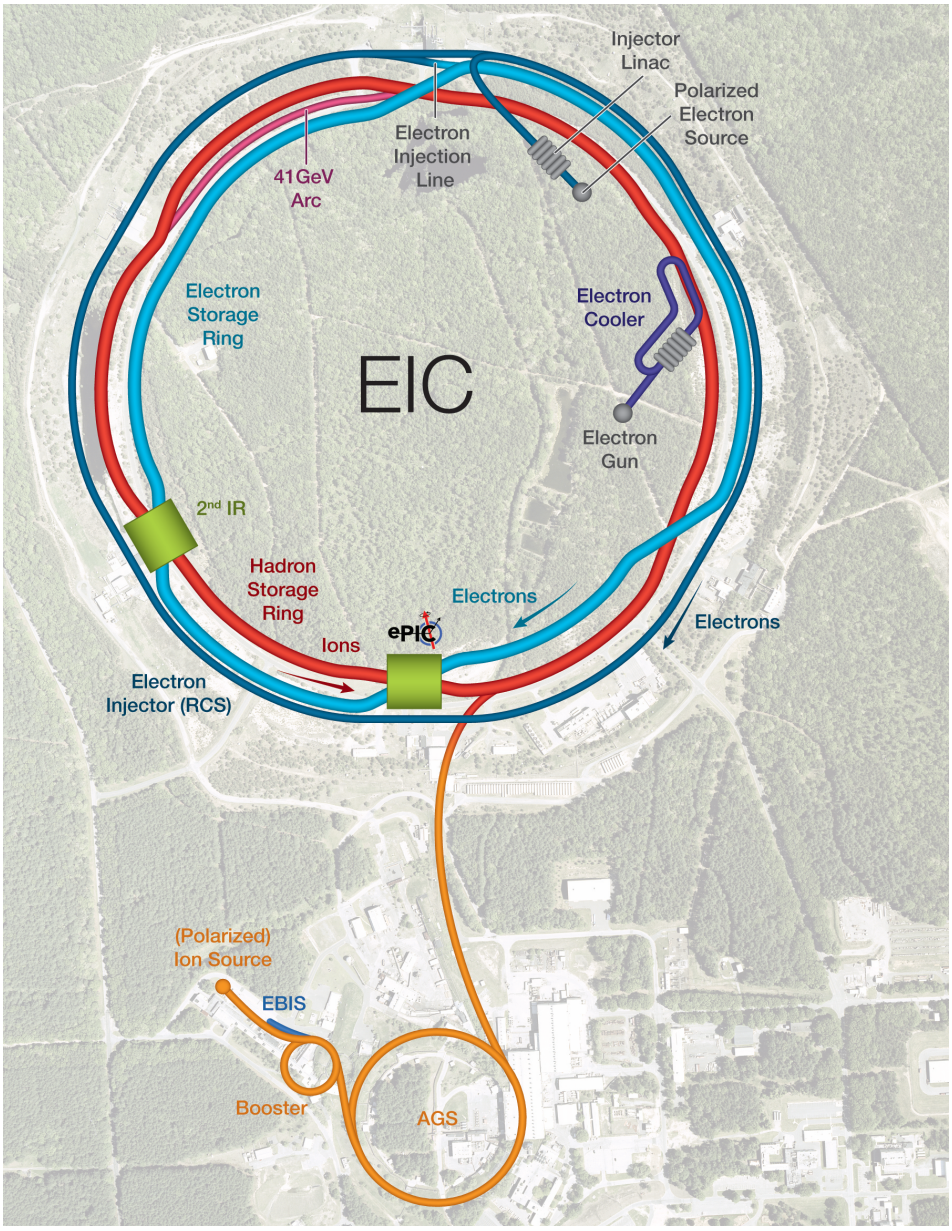

Figure 2.1: The schematic overview of the EIC Collider; the light blue ring is the ion accelerating and storage ring; the red ring is the electron storage ring; the dark blue ring is the rapid-cycling synchrotron for electron acceleration. The two interaction regions are also shown and the location of the ePIC detector is marked (courtesy of BNL Media & Communications).

2.2 The ePIC experiment

The ePIC [**ePIC**] detector is an important part of the EIC project, therefore it must be able to cope with the whole EIC physics scope [**ePICWiki**]. To this end, it has to (i) detect and identify the scattered electrons, (ii) to detect the scattered hadrons, (iii) to measure the kimetical parameters of the reaction products and (iv) to discriminate among the different hadron species.

In describing the detector, the following convention will be used: the ion going direction is referred as the forward direction, the electron going direction as the backward direction.

The detector design foresee a central detector sitting in the interaction region, long about 9.5 m, where a magnetic field of 1.7 T, for the momentum analysis, is provided by a superconducting solenoid and, on different layers, starting from the most internal ones and moving out there are a tracking system, devices for the particle identification, and electromagnetic and hadron calorimeters (FIG. 2.2. The central detector will cover an azimuthal range of -178^o - 178^o. To complete as much as technically possible the detector hermeticity, far detectors are foreseen along the outgoing beam line: in the far forward region are located tracking systems to detct particles scattered at very small angles and a hadron calorimeter, which has the capability to detect neutral particles needed for exclusive measurements. The backward region is dedicated to measure and monitor the luminosity.

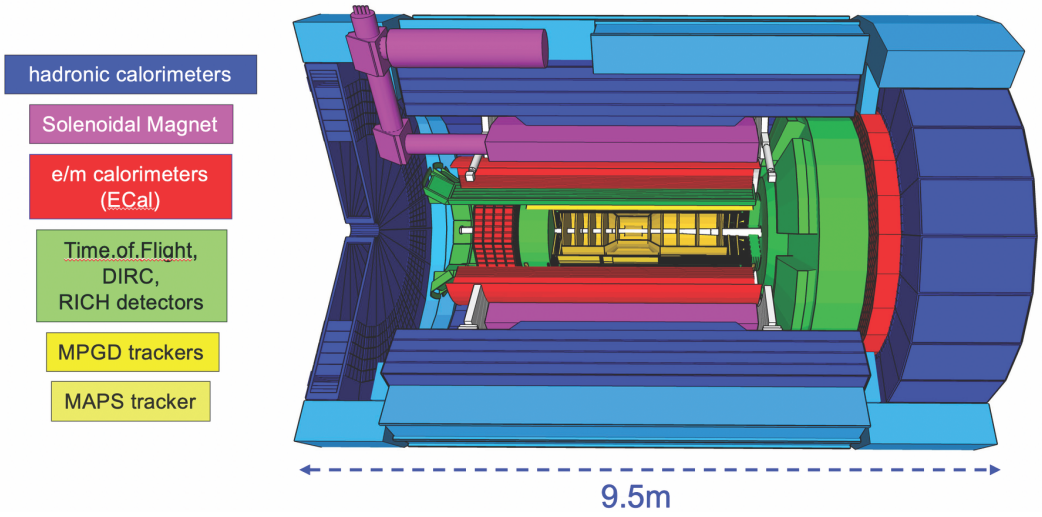

Figure 2.2: Crosscut view of the ePIC central detector. The color code identifies the different components of the detector (courtesy of the ePIC Collaboration).

The choice of the technologies and the materials is based on the requirements for the EIC physics scope.

The **tracking system** includes detectors by monolithic Si trackers and MicroPattern Gaseous Detector (MPGD) technologies. Dedicated simulation exercises confirm that the tracking and, therefore, momentum and vertex resolution is largely dependent on the material budget. The sensors selected for the Si tracking are thin, low material and low power consumption MAPS in 65 nm technology, under development for the upgrade of the LHC experiment ALICE [**ITS3**]. The thin sensors, also allowing for curved arrangement virtually support-less, the very low power consumption and the possibility of large-size sensors make possible to design the most inner layers, namely the vertex arrangement, with extremely low material of only 0.05% radiation length per layer for the three vertex layers. The same sensors arranged in a configuration with support are considered for the surrounding layers and the endcaps. The adopted MAPSs offers very fine space resolution O(10μm), but poor time information, that should be provided by complementary tracking devices. The tracking systems is completed by large-size MPGDs adopting cylindrical MICROMEGAS and the novel μR-WELL technologies. They can provide time resolution better than 10 ns.

Electromagnetic calorimetry is by different technologies in the various regions of the central detector. The high resolution required in measuring the backward scattered electrons is provided with a fine granularity crystal calorimeter by $PbWO_4$. A hybrid electromagnetic calorimeter with imaging layers instruments the barrel. Its design uses light-collecting calorimetry based on Scintillating Fibers (SciFi) embedded in lead and imaging calorimetry based on the monolithic silicon sensors AstroPix. The imaging of particle showers is achieved by four layers of imaging silicon sensors interleaved with SciFi/Pb layers, followed by a thick layer of SciFi/Pb calorimeter resulting in a total radiation thickness of about 20 radiation lengths. It is a design with the capability of detecting scattered and secondary electrons and separating them from pions, of detecting and reconstructing the full kinematic information for photons, and provide sufficient spatial resolution to identify, up to high momenta, gammas from neutral pion decays. In the forward endcap, electromagnetic calorimetry is via a matrix of tungsten powder and epoxy with embedded scintillating fibers.

Hadron calorimetry is by ion absorbers and scintillating counters as active elements. The forward calorimeter makes use of a novel approach with the sensors, which are Silicon PhotoMultipliers (SiPM) embedded in the scintillating tiles, while the signals are conveyed to the rear calorimeter face where they are collected.

Particle identification is discussed in Chapter 4.

The accelerator and detector effort are complemented by **polarimetry** requirements. Rapid, precise beam polarization measurements will be crucial for meeting the goals of the EIC physics program as the uncertainty in the polarization propagates directly into the uncertainty for relevant observables as asymmetries. The basic requirements for beam polarimetry are non-destructive with minimal impact

on the beam lifetime, uncertainty at the 1% level, the capacity of measuring the beam polarization for each bunch in the ring with rapid, quasi-online analysis in order to provide timely feedback for accelerator setting up. The electron beam polarimetry will be based on the well established Compton polarimeter techniques, where the polarized electrons scatter from 100% circularly polarized laser photons. This approach offers the advantage that both longitudinal and transversal polarizations are measured. Hadron polarimetry has been successfully performed on RHIC polarized proton beams for nearly two decades. Through continual development a relative systematic uncertainty <1.5% was achieved for the most recent RHIC polarized proton run. As the only hadron polarimeter system at a high energy collider it is the natural starting point for hadron polarimetry at the EIC. Hadron polarization will be measured via a transverse single spin left right asymmetry in the pp interaction on targets by plastic material (H-C composition), where the experimental challenge is the control of the background events.

Chapter 3

Particle Identification by Cherenkov Imaging Technique

3.1 Particle identification

In experimental particle and nuclear physics particle identification plays a crucial role. Particles can be identified by several means. One of the techniques used at high energy is to estimate the invariant mass (m) of the particle.The relativistic formulation of momentum (p) is given in equation 3.1

$$\begin{aligned} p &= m\gamma\beta c \\ m &= \frac{p}{\gamma\beta c} \end{aligned} \tag{3.1}$$

where γ, β and c carry the usual meaning of special relativity. Therefore, the mass can be determined if we can independently measure the momentum and the velocity of the particle. A magnetic spectrometer, for instance, can provide a measurement of the momentum.

The uncertainty associated in the measurement of the mass can be obtained by propagating the uncertainties in equation 3.1:

$$(\frac{\delta m}{m})^2 = (\frac{\delta p}{p})^2 + (\gamma^2\frac{\delta\beta}{\beta})^2 \tag{3.2}$$

From equation 3.2 we can see that the accurate measurement of the velocity becomes critical in the invariant mass determination for high momentum particles. In fact, the term dependent on the velocity uncertainty is enhenced by the factor γ^4.

Ring Imaging Cherenkov detectors (Sec. 3.3.1) are extremely powerful devices to provide β with fine resolution for high energy charged particles. Moreover, they can provide the measurement over a wide phase-space range. Therefore, they are powerful detectors for particle identification [**nappi2011advances**].

3.2 The Cherenkov effect

A charged particle moving in a dielectric matter polarizes the atoms and the molecules around it. If the speed of charged particle is slower compared to the speed of light in that medium, then the polarized atoms or molecules get enough time to relax before the charge is displaced. However, interesting physics appears when the charge particle is ultra-relativistic. The deformation caused by the local electric field of the charged particle is not restored before the charge moves to a new point in spacetime. This manifests into a far-field electromagnetic radiation. The radiation is emitted with speed $c' = \frac{c}{n(\lambda)}$ where c is the speed of light in vacuum and $n(\lambda)$ is the refractive index of the material at the wavelength λ of the wave. The Cherenkov effect manifests this physics. In a dielectric material a trough-going particle with speed v greater than the light speed in the material $v > c'$ generates the Cherenkov radiation [**vcerenkov1937visible**]. The radiation is caused by breaking the symmetry of the light emission, resulting in a constructing interference and in a measurable macroscopic effect. Respect to the particle trajectory, this emission is uniform in the azimuthal angle, with a polar angle θ_c that depends on the velocity of the particle. From a simple geometric calculation the Cherenkov equation results:

$$cos(\theta_c) = \frac{1}{\beta n(\lambda)} \tag{3.3}$$

Hence the measurement of the polar angle, known as Cherenkov angle, allows one to determine the velocity of the ultra-relativistic charged particle. Hence, by measuring the momentum of a particle and the Cherenkov angle, it is possible to determine its mass. The idea to identify mass of charged particles by exploiting the directional properties of the Cherenkov radiation was conceived by Roberts [**roberts1972novel**].

Two important consequences of the Cherenkov equation have to be underlined.

- There exists a β threshold $\beta_{th} = \frac{1}{n}$, namely the Cherenkov radiation is emitted only if the charged particle moving through the medium has a $\beta > \beta_{th}$. The threshold momentum depends on the refractive index of the material and on the mass of the particle. This threshold set a lower limit for direct particle identification by Cherenkov techniques.

- For $\beta \to 1$, the emission reaches a saturation angle defined as $cos(\theta_{max}) = \frac{1}{n}$,

which is the same for every particle and depends only on the refractive index. This means that different particle with high momentum emits radiation at the same angle, resulting in an upper limit in the momentum range for the particle identification.

The number of Cherenkov photons emitted at a specific wavelength is determined by the Frank and Tamm Law. For a given radiator, the number of emitted photon is proportional to $sin^2(\theta_c)$.

3.3 Cherenkov detectors

There are three main categories of Cherenkov detectors.

- **Threshold Cherenkov counters**: the emission angle is not measured, different materials with different threshold are used, each one can give a boolean signal. Knowing the momentum of a particle, different combination of boolean signals discriminate different particles. Gaseous detectors can be used varying the gas pressure, which results in varying the refractive index and, therefore, the threshold modifying the detector response.
- **Differential Cherenkov detectors**: a geometrical arrangement is used to preserve only the radiation emitted at a certain angle range. Particles with a fixed momentum emits Cherenkov radiation at an angle determined by their mass, therefore only the particles with the specific selected mass will give a signal identifying it. These devices are used is secondary beam lines to separate the particle species.
- **Ring Image Cherenkov detectors (RICH)** are equipped with a photon sensor with high spatial resolution, therefore, by analyzing the ring image generated by the passage of a particle, the Cherenkov angle can be measured [**ypsilantis1994theory**].

3.3.1 RICH

A RICH detector can either be used in a focusing or in a proximity-focusing mode. For **high momentum particle identification**, a lower value of refractive index is chosen, to allow saturation of the Cherenkov angle at larger momenta. The low refractive index results in a small number of produced photons per unit length, much smaller than for a solid state radiator. To recover a larger number of photons a long radiator is used. Therefore, the photon emission point in affected by a large uncertainty. This is cured with an optical system. Thanks to the property of a

focusing mirror, the emitted Cherenkov photons with parallel trajectories, namely the photons emitted with the same azimuthal angle at different points along the particle trajectory, are focused onto a same point on the photodetector surface. Considering photons emitted with different azimuth, the resulting image is a ring (Fig. 3.1 (a)). A focusing RICH detector is composed by three essential parts:

1. A radiator, where the Cherenkov radiation is produced;
2. A photodetector system, to collect and detect the photons emitted;
3. a set of mirrors to focus the emitted Cherenkov photons onto the sensor surface.

When the refractive index is higher, namely when **low momentum particles** have to be identified, the radiator can be thin and no focusing optics is needed. This is a proximity focusing RICH and a sensor plane is placed downstream of the radiator at an appropriate proximity gap to guarantee the formation of a ring-like image (Fig. 3.1 (b)).

The radiator selection is the first step in the design of a detector, taking into account relevant physical parameters. It's important to choose a radiator transparent in the wavelength range of the emitted photons that the selected photosensor can detect, typically the visible range or the ultraviolet region. There will be however an intrinsic uncertainty in the measurement due to the chromatic dispersion of the radiator medium. This results in an irreducible limit in the resolution of the reconstructed Cherenkov angle of the single photo-electron.

The photons emitted in the radiator must reach the photodetector, different ways can be implemented. A different approach to Cherenkov imaging devices is by the Detection of Internally Reflected Cherenkov light (DIRC). In DIRCs, quartz bars are at the same time radiators and light guides; in fact, the Cherenkov light is trapped inside the bars by total internal reflection and it travels by a zig-zag path preserving the angular information until it reaches a photodetector (Fig. 3.1 (c)).

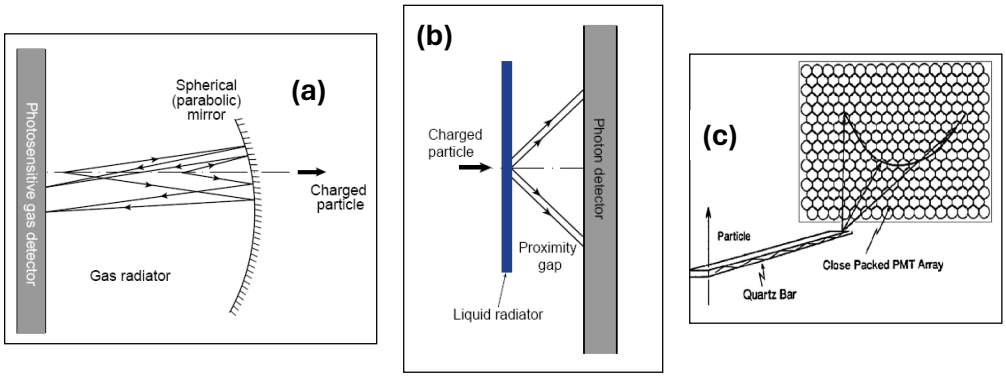

Figure 3.1: Schematics of Cherenkov imaging counters: (a) focusing RICH, (b) proximity focusing RICH and (c) DIRC.

Chapter 4

Particle identification at the ePIC experiment

4.1 Particle Identification scope and selected technologies

The Particle IDentification (PID) system of the ePIC central detector has a double mission:

- The identification of the scattered electron in the final state is crucial for the whole physics scope. It is largely based on combining tracking and electromagnetic calorimetry information. Nevertheless, also due to the high production rate of pions in a wide phase-space range of the final state, the purity of the electron sample is not as good as desired, in particular at low momenta, below a few GeV/c. The PID system can largely contribute to refine the electon-pion separation at low momenta.

- The identification of the different hadron species (π, κ, p) as required by the physics scope, in particular for the measurements of SIDIS.

The physics requirements of EIC has driven the choice of technologies for PID [**Abdul_Khalek_2022**] (Fig. 4.1). The wide range of particle momenta impose the choice of a variety of technologies. In the electron going direction (backward region), a proximity focusing RICH (pfRICH) detector and ToF provided by the phosendoe of the pfRICH, which are stting in the detector acceptance; in the barrel high performance DIRC (hpDIRC) and AC-LGAD based Time of Flight (ToF) and in the hadron going direction (forward direction) a dual Radiator RICH (dRICH) and AC-LGAD ToF has been chosen as the baseline sub-detector system to cover

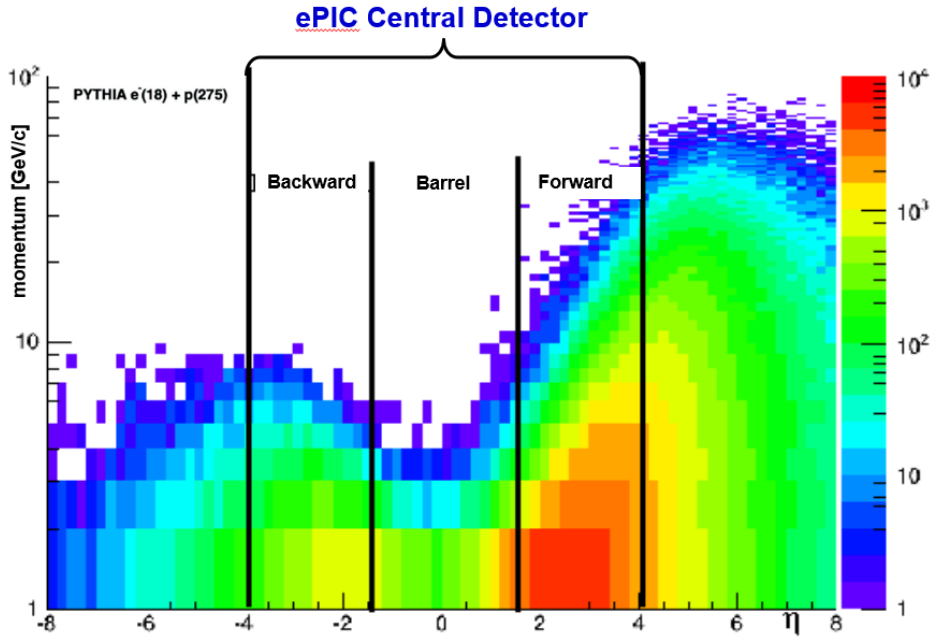

Figure 4.1: Two-dimensional distribution versus pseudorapidity and versus momentum of the hadrons from simulated DIS events (event generator : PYTHIA6: beam energies: 18 GeV electrons, 275 GeV protons.

the entire PID phase-space. The overall arrangement of the PID devices within the ePIC detector is shown in Fig. 4.3.

4.2 Backward region

The pfRICH (Fig. 4.4) uses aerogel radiator has been design so to deliver pion/kaon separation up to 9 GeV/c in the backward region, as resulting from the detector simulation studies. Despite of getting inspiration from established concepts of pfRICHes employed in other experiments (cite Belle2, AMS pfRICH), a large proximity gap is used to improve the single photo-electron (SPE) Cherenkov angle resolution. An aerogel radiator of refractive index 1.045 is assumed. High Rate Pico-second Photon Detectors (HRPPD) produced by INCOM[1] (Fig. 4.5) have been chosen as photosensors. Conical shaped mirrors are implemented in the simulation to collect the photons from particles at extreme pseudo-rapidity, which are otherwise absorbed in the beam-pipe or by the vessel walls. Thanks to fast timing response, the Cherenkov photons generated by the through going particles

[1]Incom Inc., 294 Southbridge Rd, Charlton, Massachusetts, 01507, United States

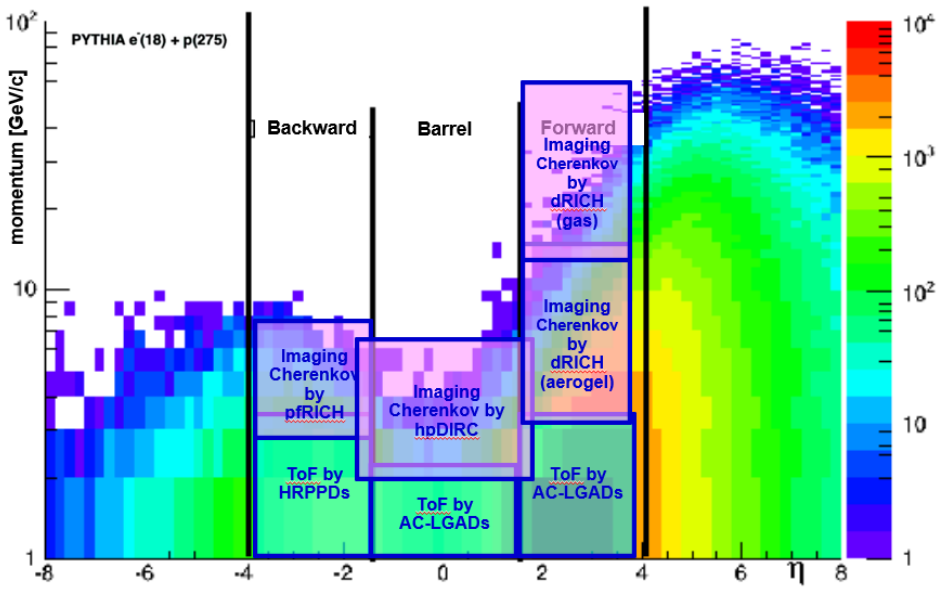

Figure 4.2: The distruction of Fig. 4.1, where the areas instrumented by the different techniques for PID adopted in the ePIC detector are shown; the areas cover the region where π/κ separation is above the 3 σ level.

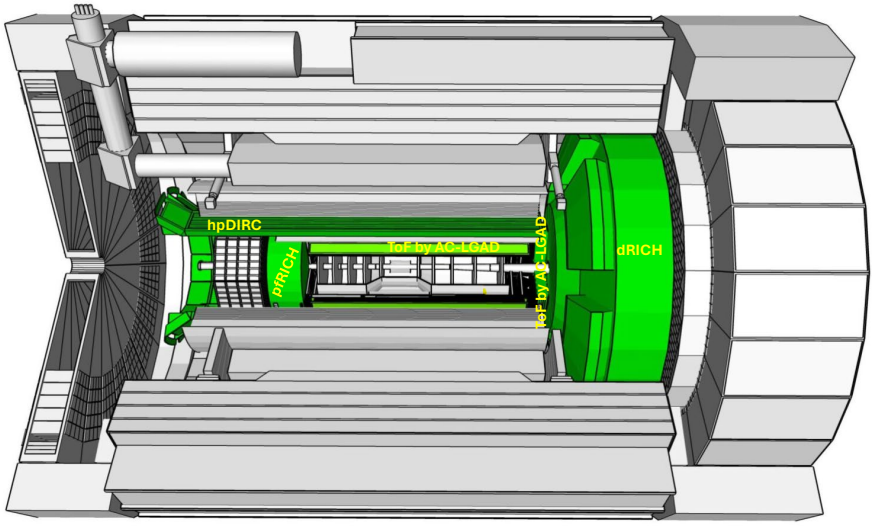

Figure 4.3: Crosscut view of the ePIC central detector. The PID devices are indicated in color.

in the fused silica (quartz) window of the HRPPDs can be used to provide a timing reference in the backward region.

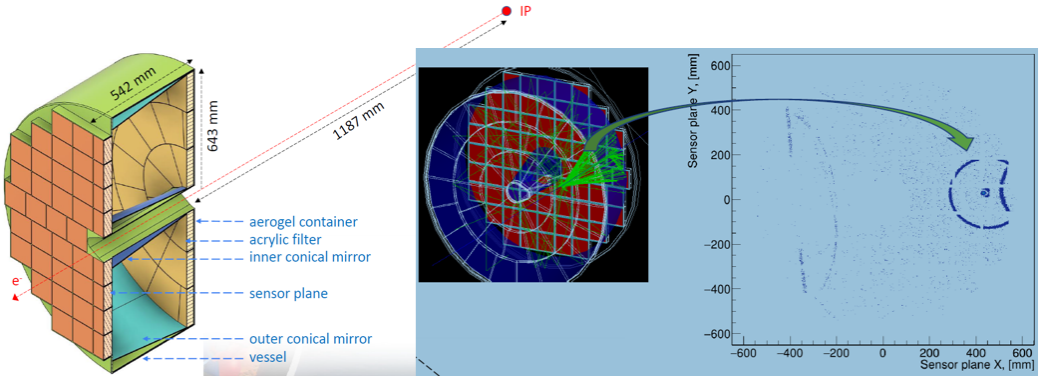

Figure 4.4: (left) Artistic view of the pfRICH. (right) Schematic illustration of the pfRICH working principle.

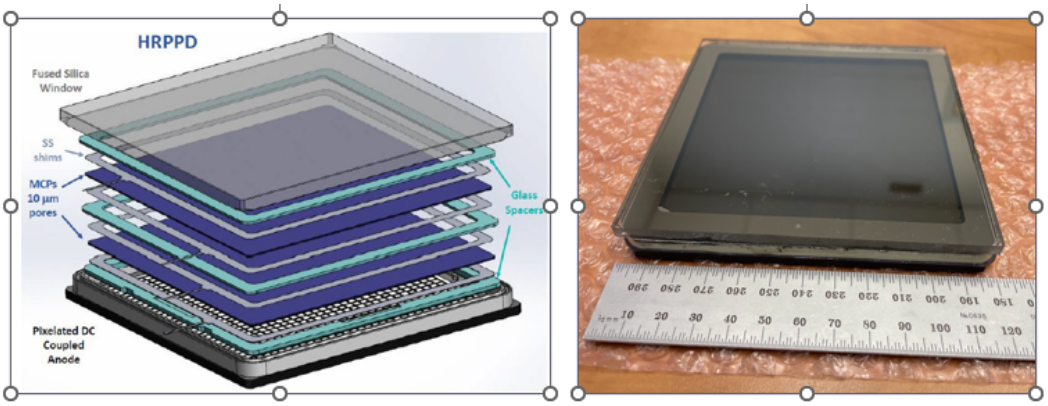

Figure 4.5: HRPPD. (left) The HRPPD components inan expanded view. (right) A picture of an HRPPD unit.

4.3 Barrel region

The PID in the barrel region will be delivered by the hpDIRC and barrel ToF based on AC-LGAD technology.

4.3.1 Time of Flight

The time of Flight detector in the barrel region envisages to use AC-LGAD based technology (Fig. 4.6, left). Low-Gain Avalanche Diodes (LGAD) are silicon sensor providing very fine space and time resolution. The modified version AC-LGAD also provides $\sim$ 100% filling factor. Strip sensor channels (500 μm x 1 mm) are considered for the barrel. Pions and kaons can be separated at 3σ limit up to

2 GeV and electron and pion can be separated up to 500 MeV in the barrel region.

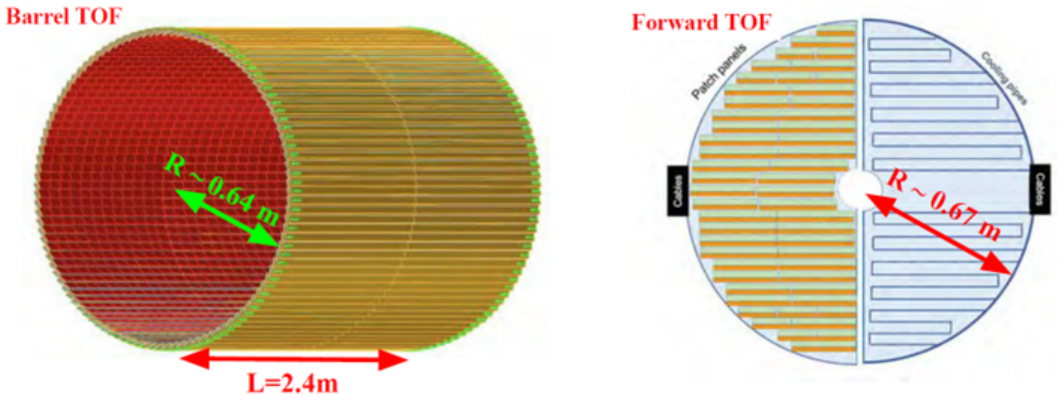

Figure 4.6: Schematics of the ToF systems based on AC-LGAD technology. (left) ToF in the barrel. (right) ToF in the forward endcap.

4.3.2 hpDIRC

A detector based on the Detection of Internally Reflected Cherenkov light (DIRC) principle, with a compact radial size of only 7-8 cm, was selected as the PID system for the ePIC barrel region (Fig. 4.7. It is anticipated to achieve a π/κ particle separation with a minimum significance of 3 standard deviations for momenta up to 6 GeV/c. This performance represents an improvement of nearly twice the current state-of-the-art DIRC systems, primarily thanks to the introduction of a 3-layer focusing lenses, small pixel sensors, and fine time resolution readout electronics. The high-performance hp DIRC (hpDIRC) is built upon the concept of a focusing

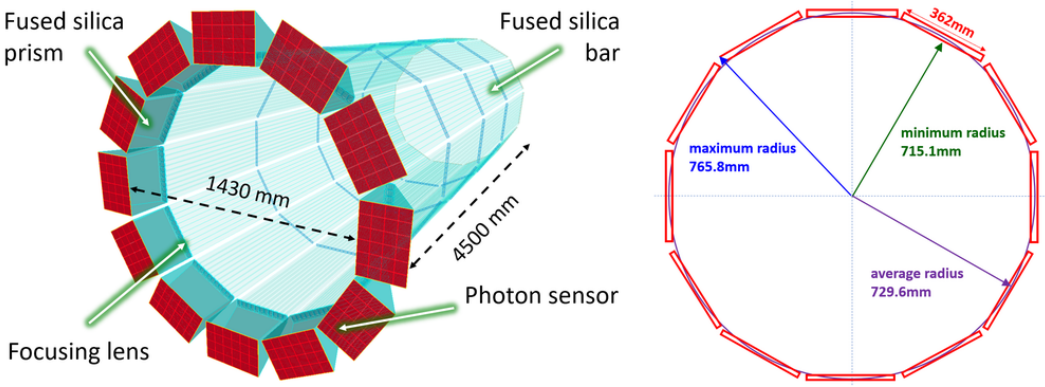

Figure 4.7: Artistic view of the hpDIRC.

DIRC detector, incorporating precise 3D (x, y, t) reconstruction. It is partitioned

into twelve optically isolated sectors, each consisting of two light-tight containers, known as a bar box and readout box, which encircle the beamline within a 12-sided polygonal barrel with a slightly greater than 70 cm inner radius. Each bar box is equipped with a series of ten radiator bars, made of synthetic fused silica, separated by small air gaps. These bars are 4600 mm in length and have a cross-sectional dimension of 17 mm $\times$ 35 mm. At one end of each bar, mirrors are affixed to redirect Cherenkov photons toward the readout end, where they exit the bar and are focused, by a 3-layer spherical lens, on the back surface of a prism that serves as an expansion volume. The prism is constructed from synthetic fused silica Each prism's backplane is covered with sensors featuring a pixel size of approximately 3 mm $\times$ 3 mm, enabling the recording of Cherenkov photons' position and arrival time. The designated sensor solution for the hpDIRC's baseline design consists of commercial MicroChannel plate PMTs (MCP-PMTs) with a pore size of 10 µm or less, available from Photek or PHOTONIS. A comprehensive standalone Geant4 simulation was developed together with the PANDA Barrel DIRC group and validated with particle test beam data.

4.4 Forward region

Particle identification in the forward region is performed by a Time of Flight (ToF) system and a dual radiator RICH (dRICH).

4.4.1 ToF

In the forward region also a AC-LGAD based time of flight detector is envisaged (Fig. 4.6, right). Contrary to the barrel region, a (500 μm x 500 μm) pixel channel configuration is considered. In the forward region 3-σ pion-kaon and electron-pion separation can be achieved up to 2.7 GeV and 800 MeV respectively.

4.4.2 dRICH

A dRICH employs two radiators to cover a wide momentum region, possible with a substantial overlap. The baseline dRICH (Fig. 4.8) has been designed with aerogel, 4 cm thick with refractive index 1.02, and 1.2 m of C_2F_6 radiator gas; the two radiators, respectively, provide PID for the lower and higher momentum regions. The RICH design is based on the replica of six identical arrangements of mirrors and a spherical phosensor sectors. Each mirror focuses the reflected photons onto the corresponding photosensor area. The dRICH covers the pseudorapidity range (1.5, 3.5).

SiPM are used as detector of single photons. These Si sensor are matrices of micro pixels, which operate in Geiger mode. The choice of this detectors is a

challenge because SiPMs are affected by relevant dark counting rate and, because of the Geiger operation mode, the dark discharges are identical to the signals generated by the conversion of a single photons. The dark count rate is mitigated operating the SiPMs at low temperature (O(-40^{o}C)). The Dark counts increase due to radiation damage. The SiPMs have been qualifies as adequate detector for the use in the dRICH via a robust R&D program. The increase of dark counting rate has been measured for given fluences. The recovery obtained with thermal cycles at high temperature has been determined and confirmed in repeated cycles alternating irradiation and annealing. The possibility to perform the SiPM annealing in situ by heating with the application of reversed voltage bias has also been proven. It has been established that, at ePIC, the SiPMs used in the dRICH will not go beyond the rate of 300 kHz per SiPM unit. Assuming a time opening window of 1 ns for the read-out of the information related to a physic event, this correspond to a probability of $\sim 3 \cdot 10^{-4}$ of a noise hit per SiPM, which results in $\sim$100 noise counts per event in the whole read-out system consisting of $3 \cdot 10^5$ SiPMs.

An extruded sensor box hosts the spherical sensor planes with 10 cm attached services (including Front-end electronics, cooling and back-end services). This systems provide the entire acceptance of the dRICH. Each Photon Detection Unit (PDU) is grouped into 2X2 matrix of photosensitive surfaces with a 0.2 mm gap. Each sensor surface contains 4X4 SiPM pixels of 3 mm. Therefor a total of 64 pixels are present in a PDU. Realistic parameters for the Rayleigh scattering, absorption length of the aerogel has been obtained from CLASS-12 aerogel parameters.

The configuration has allowed to achieve a comfortable momentum overlap with the aerogel, and a 3σ π/κ separation up to $\sim$50 GeV/c in the most demanding high pseudo-rapidity region. Three variables parameterize the spherical mirrors: the z position of the backplane, which is the maximum z the spherical mirror will reach, along with two focus tune parameters f_x and f_z. The simulation studies are in agreement with beam test performed with dRICH prototypes.

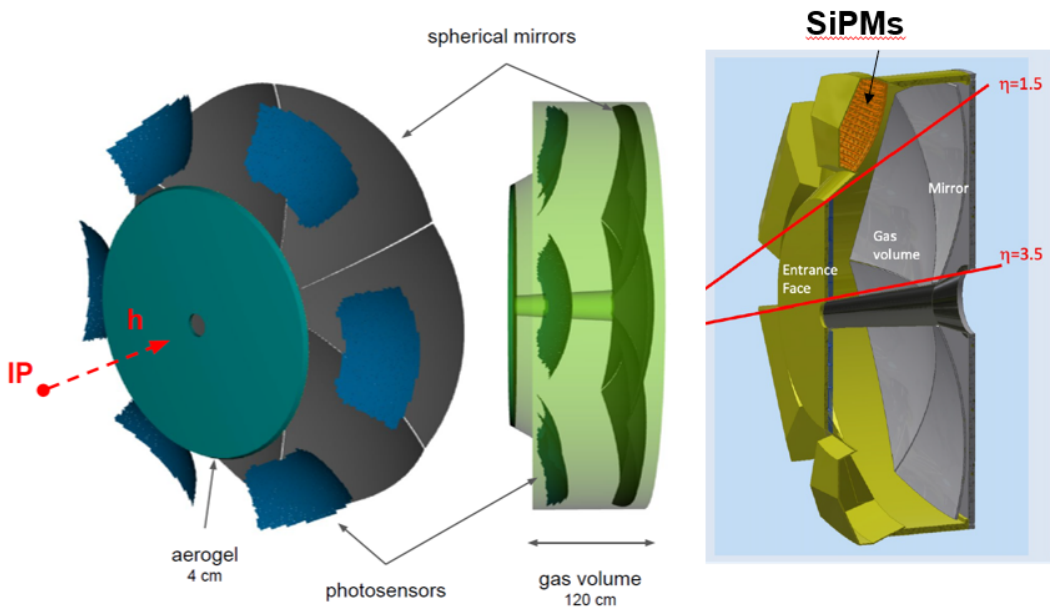

Figure 4.8: dRICH. (left) Artistic view of the dRICH. (right) dRICh from the mechanical drawings by CAD.

Chapter 5

Simulation studies with dual Radiator RICH at ePIC experiment

In this chapter I discuss the simulation study I have performed with the ePIC software scheme. The software framework and the reconstruction algorithm are briefly introducing in Sec.s 5.1 and 5.2.

5.1 Simulation software scheme

A simplified block diagram of the ePIC software scheme is presented in Fig. 5.1, where an event can be either a single generated particle or a complete physics event produced with a physics event generator. These simulated events are used as an input to the simulation. The relevant information from the event simulation is saved in the format dictated by the Data Model. The reconstruction algorithm (for dRICH described in Sec. 5.2) operates on the data producing an output in the form of Benchmark Plots. My own original contribution is by analysing the Benchmark Plots and producing the corresponding result (blocks in colour in Fig. 5.1).

5.2 dRICH Reconstruction software: IRT

The dRICH single photo-electron Cherenkov angle reconstruction is based on the Inverse Ray Tracing (IRT) method. Knowing the coordinates of the digitized photon hits and assuming a point of the photon emission along the particle trajectory inside the radiator make it possible to estimate the polar and azimuth angle of the emitted photons.

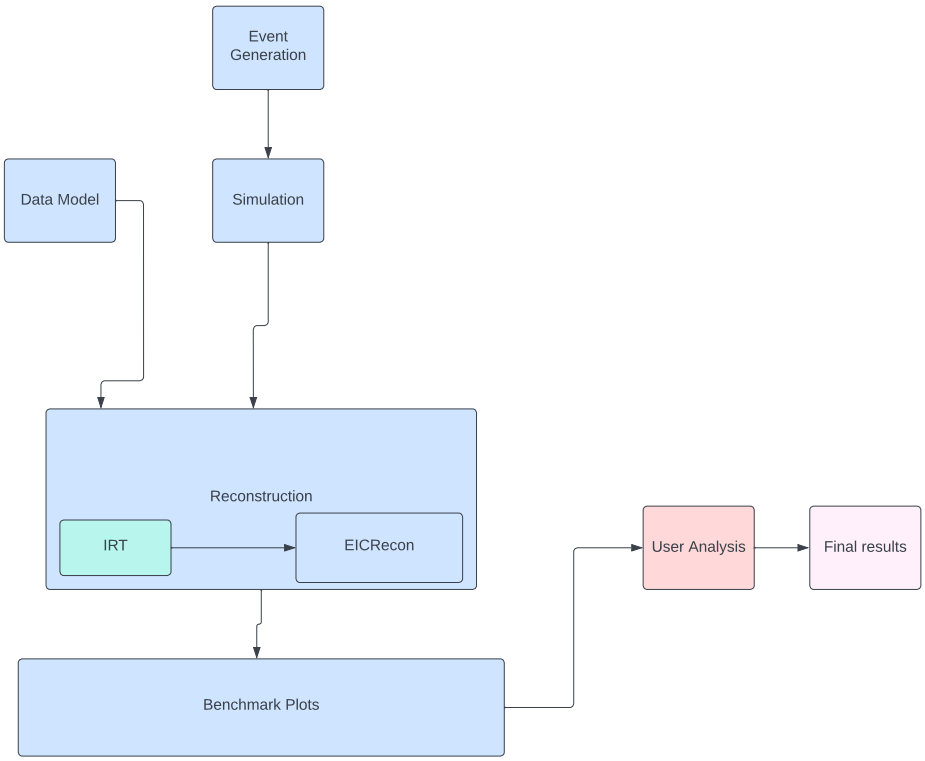

Figure 5.1: Block diagram of the simulation scheme of the ePIC experiment.

For the implemented version in ePIC, a set of emission points along the particle trajectory are assumed from the projection of the reconstructed tracks inside the radiator. Each of these assumed emission points returns a value of the Cherenkov angle. Thanks to the good parallelism, for a given azimuthal angtle, of the Cherenkov photons along the trajectory and to the focusing properties of the mirror, these values are close to each other. An average values of the estimated angles obtained from each of the used track points is assumed. In a simplified approach, the assumption that the photon has been emitted from the mid-point of the track should serve the purpose of the Cherenkov angle reconstruction; however, in case of the presence of the magnetic field, which is the case for the dRICH in ePIC, the bending of the track adds extra complexity. This can be overcome by taking into account, in the track reconstruction, the bending of the particle trajectory in the magnetic field. The effect of the magnetic field will be more relevant for the azimuthal angles of the photons in the trajectory bending plane when compared to the photons out of the bending plane. A simple schematic of the IRT scheme is shown in Fig. 5.2.

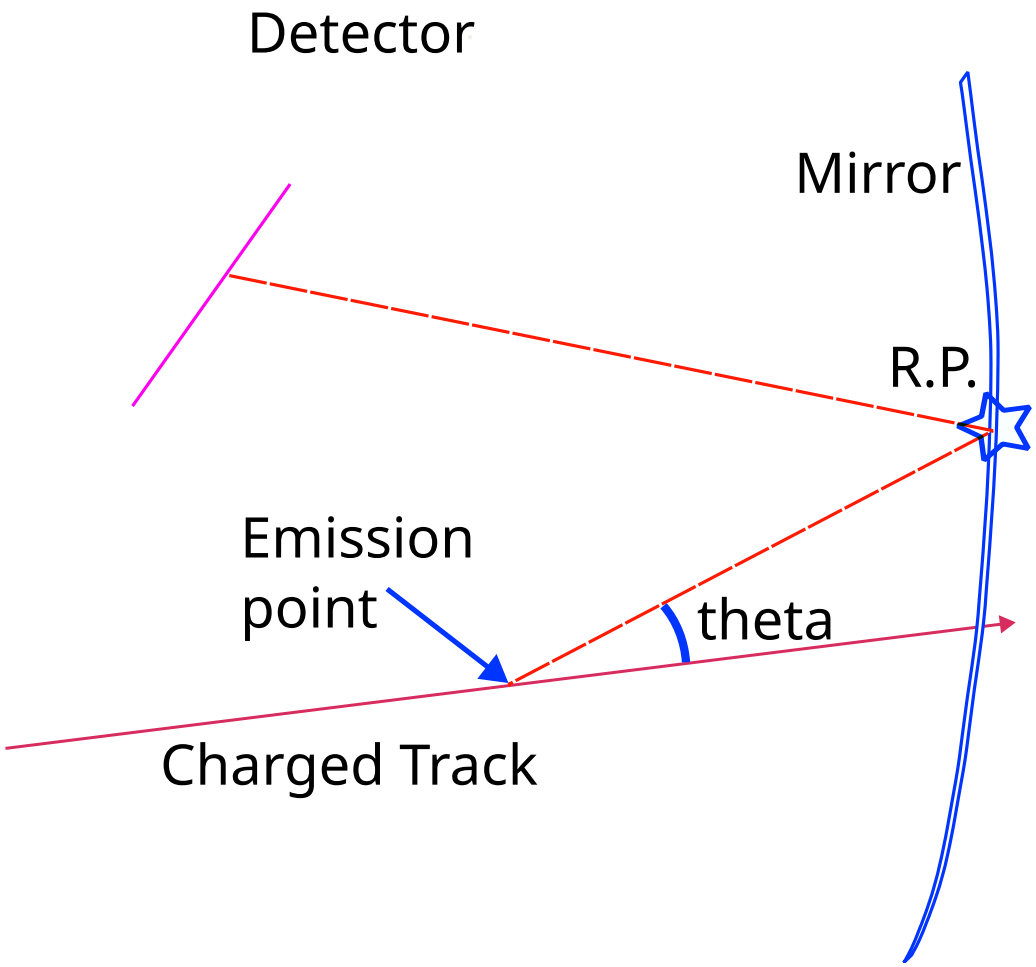

Figure 5.2: A schematic diagram demonstrate the working principle of Inverse ray tracing.

5.3 Optimization of aerogel parameters

The aerogel radiator of the dRICH provides low momentum particle identification where the momentum of the charged particles is below the momentum-threshold for Cherenkov radiation in the gas radiator. Considering π-κ separation, the EIC physics requires at least 3σ separation starting from a momentum of few hundred MeV/c to 50 GeV/c. The momentum-threshold for positive identification of the kaons in the C_2F_6 radiator is ~ 12 GeV/c. In order to have a substantial overlap with the gas radiator the aerogel, therefore, has to provide 3σ separation well above 12 GeV/c. The aerogel radiator also plays an essential role in electron identification by suppressing the contamination coming from the pion production (see Sec. 4.1).

5.3.1 Different materials

Currently the nominal aerogel thickness is 4 cm and the nominal parameters used in the simulation studies are taken from CLAS12 aerogel parameterizations (cite CLAS12 aerogel). The nominal aerogel has an average refractive index of 1.019. In this study the parameters of a new aerogel sample have been used and a comparative performance study of the current aerogel has been made. The average refractive index of the new aerogel is 1.0256. To be consistent with the parameters of the nominal aerogel, wavelength dependency of all the optical properties of the new aerogel has been extrapolated up to 1000 nm. In fig. 5.3 the parameters of the old and new aerogel samples are presented. The essential ingredients of a radiator selection mainly include the high Cherenkov photon yield, and optimized optical properties in the dynamic range of photon detection efficiency of the sensor. The Cherenkov photon yield depends mainly on: the length of the radiator, the refractive index of the radiator, its transmitence in the working wavelength range of the photon sensors. An aerogel radiator with refractive index higher than the nominal one helps in gaining more number of photons; hence a better pattern recognition can be made. Better optical properties with optimized Rayleigh scattering length improve the resolution of the reconstructed single photo-electron Cherenkov angle.

To compare the number of detected photons from the two aerogel samples, 1000 single particle events were simulated. The number of detected single photon follows a Poissonian statistics. Therefore, the average number of detected photons is estimated with a Poisson fit on the number of detected photon distribution as is shown in Fig. 5.4.

The new aerogel with higher refractive index and better optical properties outperforms the nominal aerogel in terms of detected photons in the entire phase-space. The increase in the number of detected photons can be seen as a function of momentum and pseudorapidity. An increase of $\sim$50% compared to our nominal aerogel. The performance of the two aerogel radiators as a function of momentum

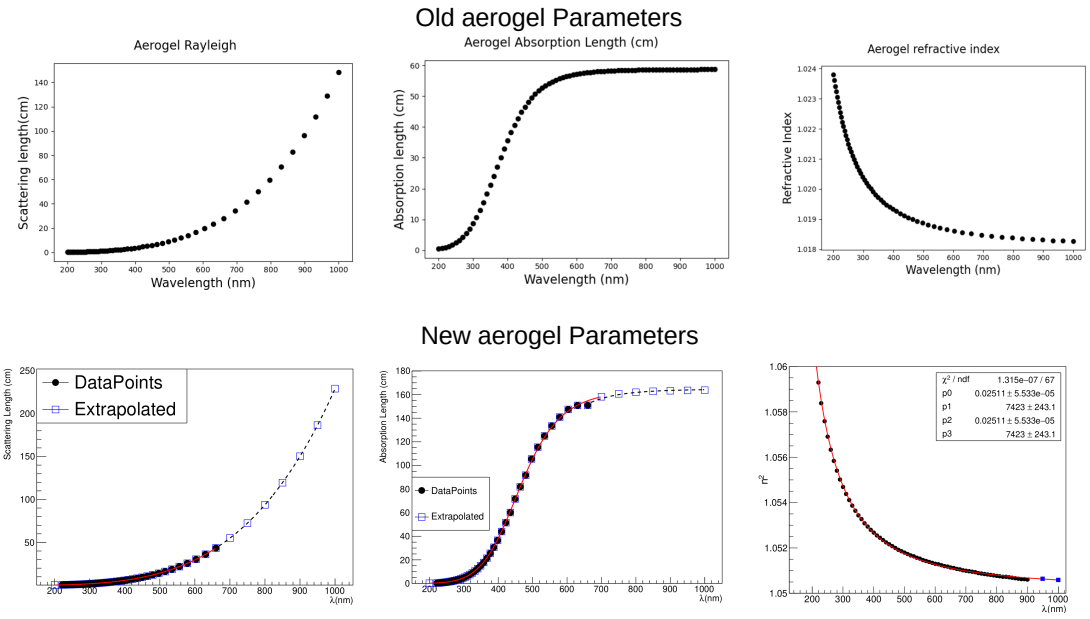

Figure 5.3: The optical parameters of the Clas12 ("old") aerogel (top) and new (bottom) aerogel.

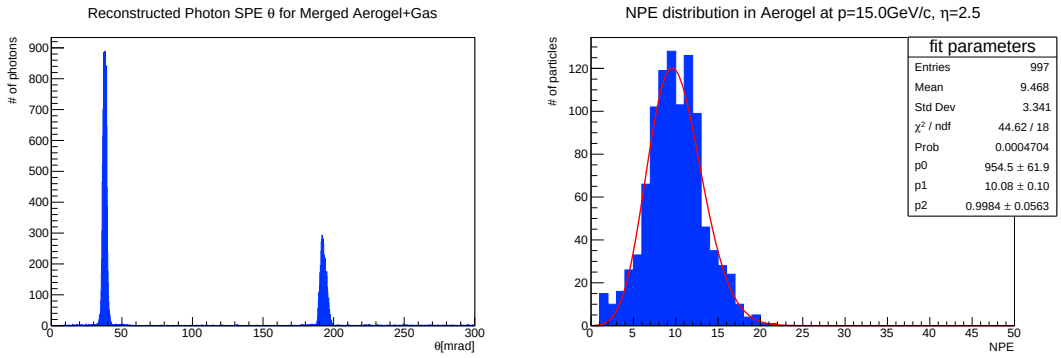

Figure 5.4: Simulation made with 1000 single pion events with momentum 15Gev/c, at $\eta = 2.5$. Left: Cherenkov angle (θ_c) distribution of the single photons, where two peaks are clearly visible: the one at smaller angles corresponds to the photons generated in the gas radiator, the one at larger angles is from the aerogel. Right: The histogram of the number of detected photons per pions coming from the aerogel is fitted with a Poissonian distribution.

is plotted in figure 5.5.

Due to geometric effects, the number of detected photons depends strongly on the pseudorapidity of the charged particle. Namely, at different polar angles the

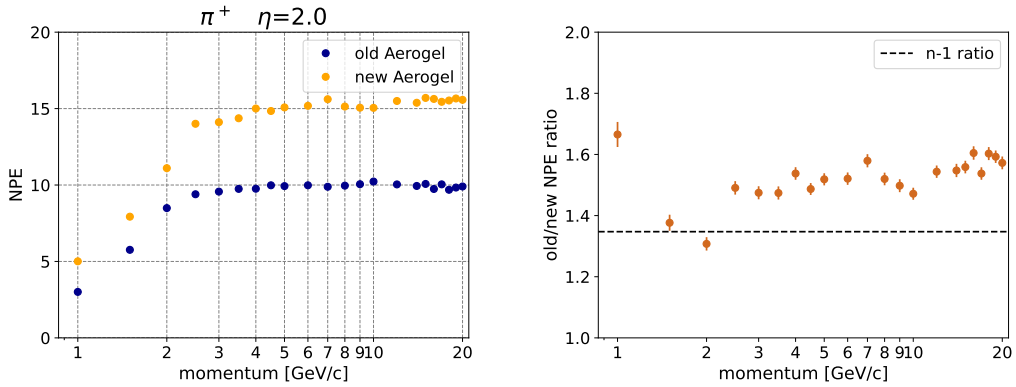

Figure 5.5: Left: Number of detected photon generated by the passage of a pion at η=2 in 4 cm of the old and new aerogel versus momentum. Right: The ratio of the number of photons as a function of momentum.

particle crosses different path lengths, leading to a different number of generated photons. It further convolutes with the acceptance of the detector. At extreme values of η a large fraction of the photons can be lost (Fig. 5.6) due to the acceptance or by the shadow created by the beam-pipe.

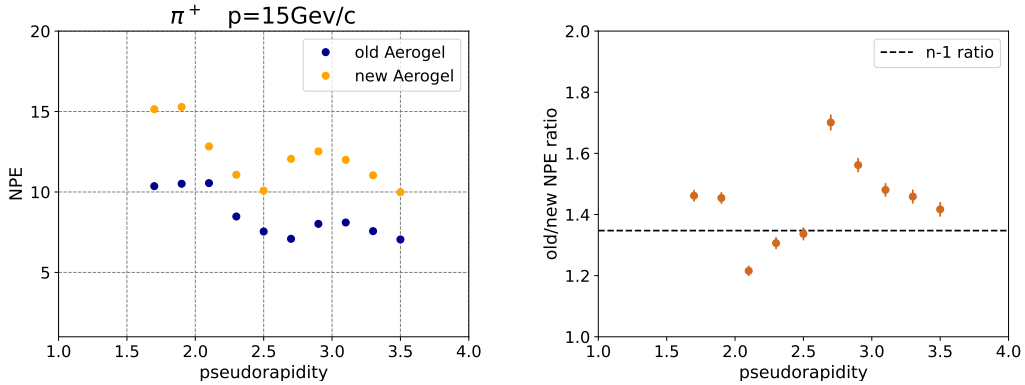

Figure 5.6: Left: Number of detected photon generated by the passage of a 15 GeV/c pion in 4 cm of the old and new aerogel versus pseudorapidity. Right: The ratio of the number of photons as a function of pseudorapidity.

The trend observed in the left plot of figure 5.6 is dictated by such convoluted effect. The simulated particles have trajectories pointing to the centre of one sector. In this case, at small pseudorapidity, the available sensor surface do not fully contain the ring. At $\eta = 1.5$ no photon is detected because of the aerogel acceptance limit. Around $\eta = 2.0$ the ring produced by the aerogel is fully contained in one sector

of photon detectors. Increasing even more the pseudorapidity, the ring start to get split into different photon detector sectors; as they are reflected by the nearby mirrors. Also a significant fraction of the photons are lost due to the shadow of the beam pipe (Fig. 5.8). The combination of the shadow of the beam pipe and the split rings generates a modulation in the number of detected photon-electrons as a function of pseudorapidity of the particles near to Cherenkov angle saturation. Given the different ring size the minima of this modulation is not at the same pseudorapidity for the two aerogel samples (Fig. 5.6). This observed effect is minimized for low momentum particle as demonstrated in figure 5.7. The ring radius for such particles is small enough that it can be contained mostly in one sector of photon sensors.

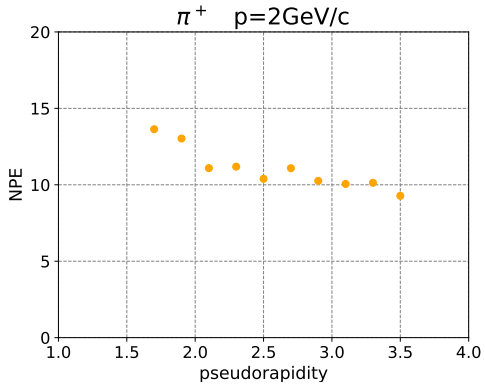

Figure 5.7: Number of detected photon generated by the passage of a 2 GeV/c pion in 4 cm of the new aerogel versus pseudorapidity.

We have also simulated events with pions and kaons samples and compared the π-κ separation (Fig. 5.9). The number of sigma separation is given by [**nappi2011advances**] in the equation 5.1

$$N_\sigma = \frac{\theta_\pi - \theta_\kappa}{(\sigma_\pi + \sigma_\kappa)/2} \tag{5.1}$$

The symbols θ_j,σ_j represent the Cherenkov angle and its resolution of the j^{th} hypothesis based on all the detected photon forming the ring, often indicated as "ring angle" and "ring resolution". We have computed the average Cherenkov angles for pion and kaon hypothesis using a Gaussian fit and extracting the central values from the fit. To estimate the ring resolution, we have fitted a Gaussian to the residual distribution of the Cherenkov ring angle, assuming the mass hypothesis of the simulated particles and the standard deviation of the fit is extracted. The ring resolution improves with momentum up to the saturation when the number of

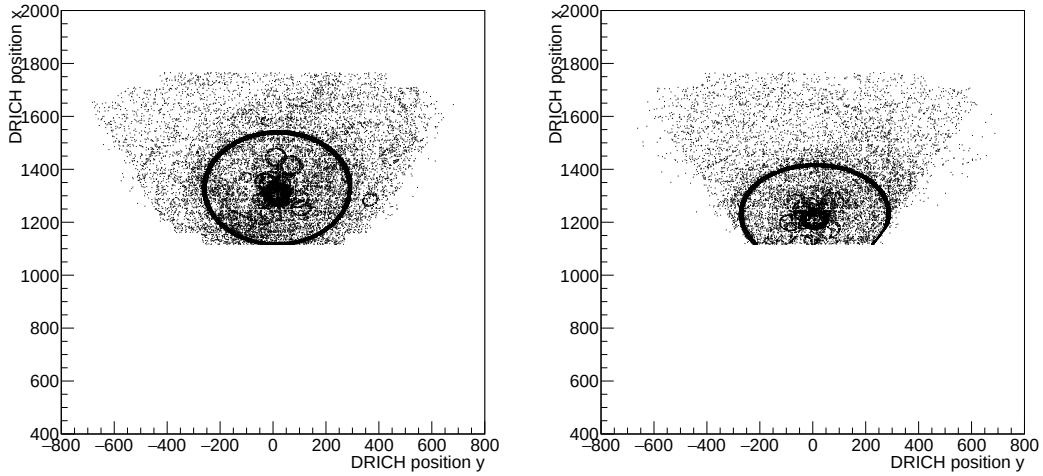

Figure 5.8: Hit maps for the detected photons from new aerogel for 1000 pions at p=15GeV/c, fixed Φ and $\eta = 2.0$ (left),$\eta = 2.5$ (right).

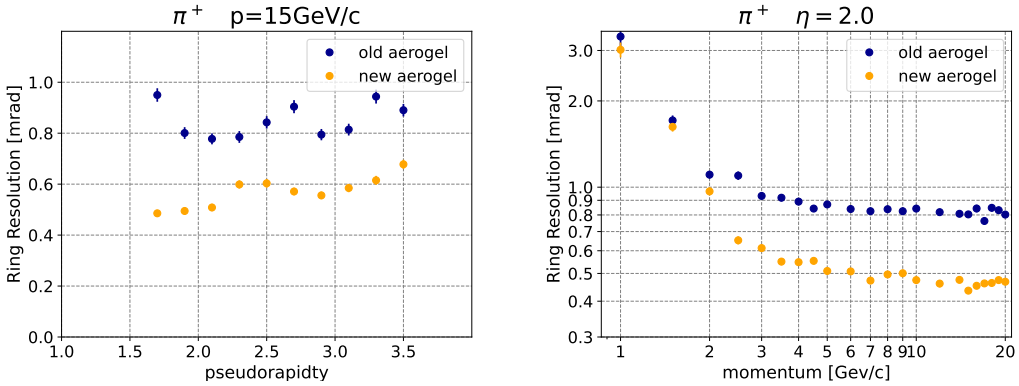

Figure 5.9: Pion ring resolution at different η and momentum with old and new aerogel parameters.

photons is constant, while for the pseudo-rapidity plot the shape is more complicated mainly due to the role played by the acceptance. It is however evident that for the new type of aerogel the resolution is better and, therefore, the number of sigma of separation is larger at a given momentum. In Fig. 5.10, we notice that the momentum limit for 3σ π/κ separation of the new aerogel surpasses the old aerogel and it goes up to 18 GeV/c; this is thanks to a larger number of photons and the better optical properties, which improve the reconstruction of single photo electron Cherenkov angle.

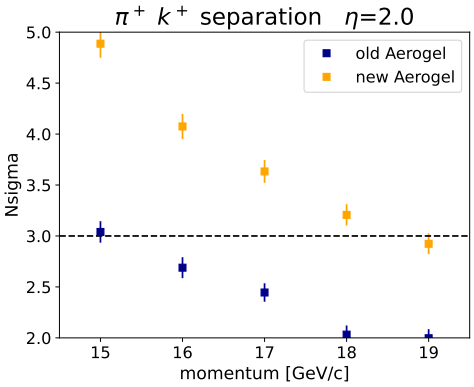

Figure 5.10: π/κ separation versus momentum for the two aerogel samples.

5.3.2 Increased aerogel thickness

To further increase the number of detected photons, we can increase the thickness of the radiator. Larger number of detected photon improves the pattern recognition and a better ring resolution can be obtained. This will further improve the 3σ π/κ separation limit. Assuming the new aerogel parameters, 1000 pions events

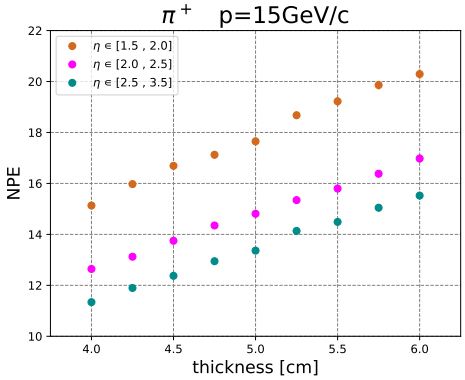

Figure 5.11: Number of detected photons versus the thickness of the new aerogel sample evaluate for three η ranges.

have been simulated at different thicknesses from 4.00 cm up to 6.00 cm, for three different pseduorapidity ranges to cover all the detector acceptance. The number of detected photons increases linearly with the thickness. Comparing the old aerogel with nominal thickness of 4 cm and 6 cm thick new aerogel, there is almost an increase of a factor 2 in the detected photos (Fig. 5.11). The ring resolution improves by $\sim 20\%$ with a 2 cm increase of the radiator thickness. The dependency of the number of detected photons and of the ring resolution as a function of

pseudorapidity and momentum can be seen in Fig.s 5.12 and 5.13, respectively.

An improved ring resolution is one of key the ingredients for a better PID performance at a higher momentum. In figure 5.14 a comparative performance of the new aerogel type at two different thicknesses are shown. In all pseudorapdity ranges a gain of $\sim 1.5\ GeV/c$ in the momentum limit for the $\pi - \kappa\ 3\sigma$ separation is observed.

Production of a single block of 6 cm thick aerogel with similarly optimized optical properties is however technically challenging. The optimization of the optical properties are achieved at smaller thicknesses. Multiple layers of aerogel tiles can be used. This introduces an irreducible surface effect that can cause a loss of detected photons. Further simulations have to be performed in future with aerogel of multiple layers in order to quantify the losses coming from the surface effect.

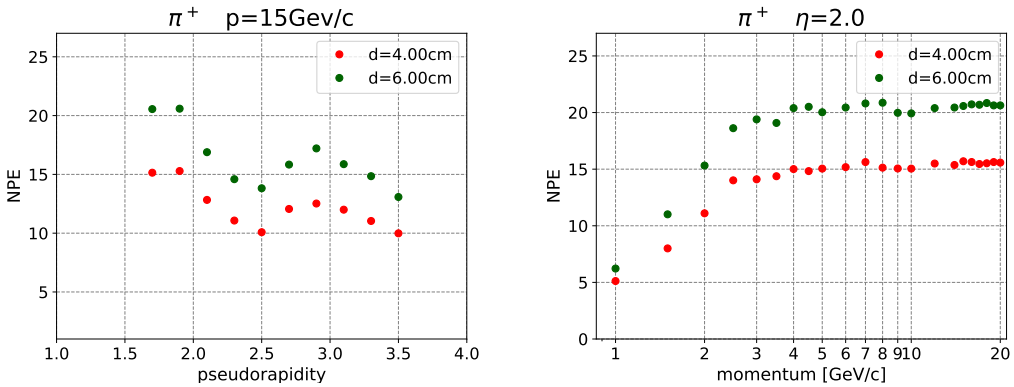

Figure 5.12: Number of detected photons versus pseudorapidities and momentum, new aerogle with thickness 4cm and 6cm.

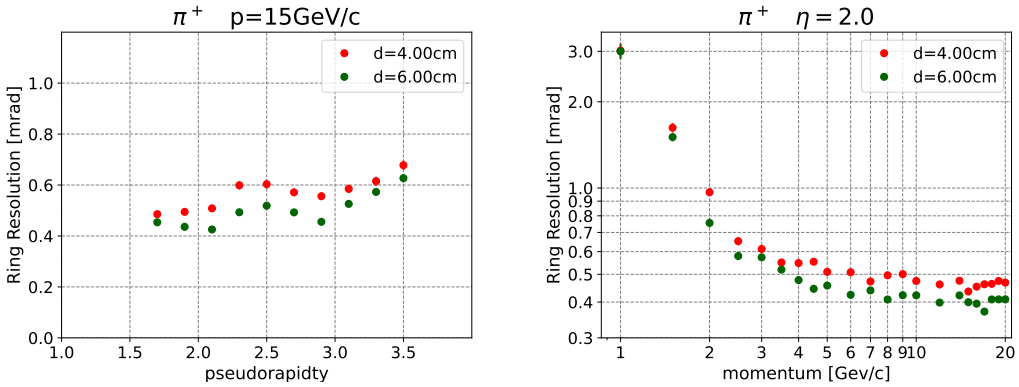

Figure 5.13: Ring resolution versus pseudorapidities and momentum, new aerogle with thickness 4 cm and 6 cm.

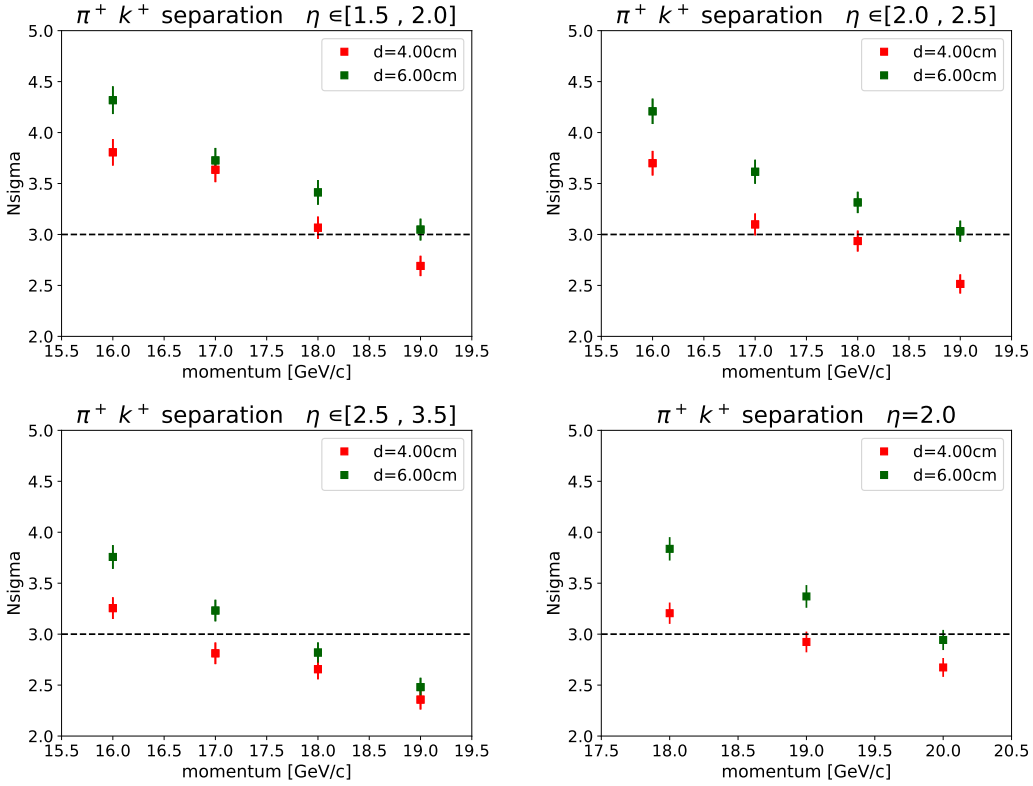

Figure 5.14: π/κ separation in three different pseudorapidity bins and in the optimal case of $\eta = 2.0$, new aerogel with thickness 4 cm and 6 cm.

5.4 Photon impinging angle on the photo sensor surface

A key property of photosensors is their Photon Detection Efficiency (PDE), which is, in general, a function of the photon wavelength and it is provided within the sensor specification.

A high PDE is essential for an efficient performance of a RICH detector. Generally speaking, in experimental determination of the PDE, a beam of photons with known flux is impinged perpendicularly to the sensor surface. However, photon beams impinged on the sensor surface at a different angle have a finite probability to be reflected back from the sensor surface and, therefore, not get detected. The impinging angle is defined as the angle between the normal direction to the sensor surface and the incident photon. The impinging angle effect can be substantial, if the shape of the window protecting the sensor is far from being planar. Therefore, using given PDE values may not fully simulate the reality. The shape of the window material on our sensor surface is not known in detail and the PDE values currently used for the SiPM only consider orthogonal incidence. A simple schematic image in Fig. 5.15 shows the situation.

This simulation study aims to estimate the maximum incidence angle of the Cherenkov photons on the sensor surface in different dRICH phase-space regions to guide the future laboratory exercises dedicated to study the dependency of the PDE versus the photon impinging angle. For dRICH, the optimized focusing of the mirror on the sensor plane is based on parallel-to-point focusing. Parallel beams of Cherenkov photons generated in the radiator along the trajectory get reflected by the mirror on a pixel of the sensor surface. At higher pseudorapidity, the majority of the final state particles have high momentum; this requires better single photo electron reconstruction resolution and hence an optimized focus tuning. The geometric constraints coming from the ePIC detector makes the focalization challenging. As a side effect to this, at high pseudorapidity the normal to the sensor surface is no more parallel to the reflected photon beams. At a lower pseudorapidity however the high momentum coverage is less critical, geometrically close parallel incidence can be preserved, but the ring resolution is worsen due to the spherical aberration.

The sensors and the mirrors are symmetric in azimuth. As a first exercise, to check all the possible impinging angle for the photons we have fixed the particle azimuthal angle at the production vertex and we have varied the polar angle of the particle. At all pseudorapdities we have used saturated particle momentum in order to have the same Cherenkov emission angle for every particle. We have simulated 1000 pions at 50GeV to ensure saturation in both the radiators (Fig. 5.16).

The dRICH is designed to work in the pseudorapidity range between 1.5 to

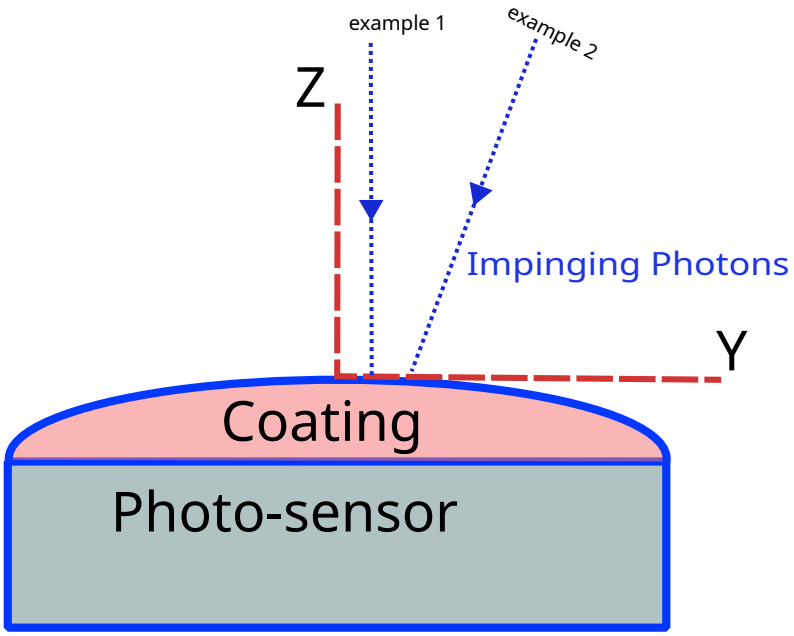

Figure 5.15: Conceptual scheme: photons impinging on the sensor surface, large impinging angle may result in photon losses to due reflection.

3.5. We took four pseudoradpidity values, within the dRICH acceptance range to study the dependency of the impinging angle of the photons generated in both the gas and aerogel radiator. In Fig. 5.16 we see the photon impinging angle as a function of the local X-Y coordinates of the photon sensor surface. The polar angle of the particle is varying along X axis (the lower the X value, the closer the photons are to the beam-pipe). The movement of the ring towards smaller values along the X axis is expected at higher pseudorapidities. The ring will however be symmetric along the Y direction. The improved ring resolution observed at larger pseudorapidity is the result of the optimization of the focusing for these phase-space region. Furthermore, the azimuthal dependency of the impinging angle can be explained in the following manner: the sensor elements are placed on a spherical surface, which is approximated with a set of small facets, not all of them having the most favourable orientation.

From the simulation exercise the impinging angles can be seen as large as 25° for the gas ring (Fig 5.16) and 40° (Fig. 5.17) for the aerogel ring, at maximum pseudorapidity of 3.5.

At pseudorapdity value of 2.0 the aerogel ring is fully contained in one sector even when the ring size gets saturated. The aerogel ring saturates for pions at around 5 GeV/c. In Fig. 5.18, the impinging angle of photons coming from the

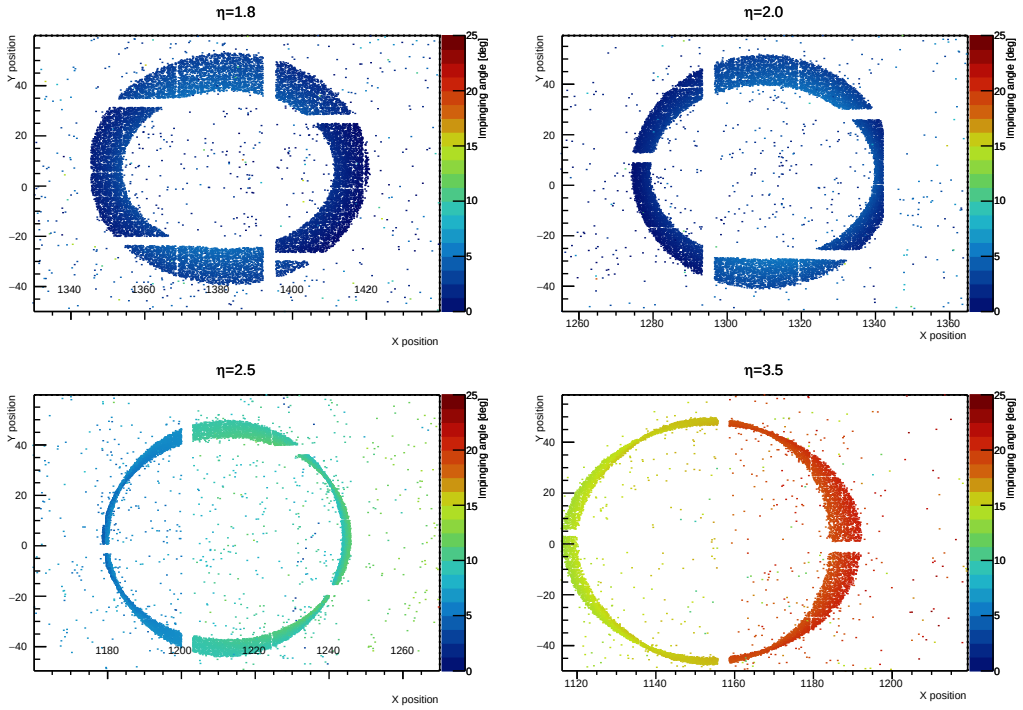

Figure 5.16: Gas ring images generated by pions at 50GeV/c and different pseudorapidity. The color scale represents the impinging angle of the photons in degrees.

aerogel is shown for different momentum values. We can see that, at 1 GeV/c the ring is split into two neighbouring sensor sectors, due to the bending of the track in the magnetic field. In this case, the maximum impinging angle is estimated to be around $\sim 30°$. For the photons generated is the gas radiator a similar study has been done at different momentum values for two different pseudorapidities for 1000 single pion events. The dependency can be seen in Fig. 5.19. The ring radius increases with momentum and finally saturates around 10 GeV. The impinging angle does not depend on the momentum. The position of the ring at low momentum is affected by the presence of the magnetic field of the ePIC solenoid.

For low momentum pions (around 1 GeV) the loss in the number of photons due to large impinging angle can cause severe limitation in the detector performance. If in the future, from laboratory exercises, a strong dependency in the number of detected photons with photon impinging angle is observed a further optimization of the dRICH detector will be necessary.

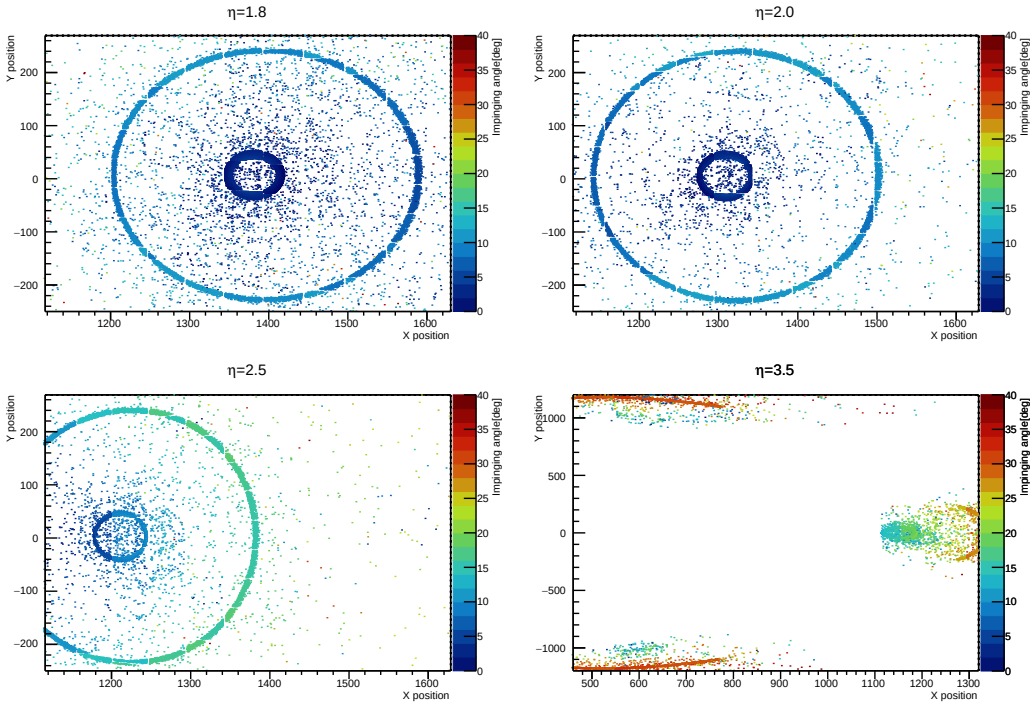

Figure 5.17: Gas and Aerogel ring images generated by pions at 50 GeV/c and different pseudorapidity. The color scale represents the impinging angle of the photons in degrees. At η=3.5 the aerogel ring is split among different dRICH sectors.

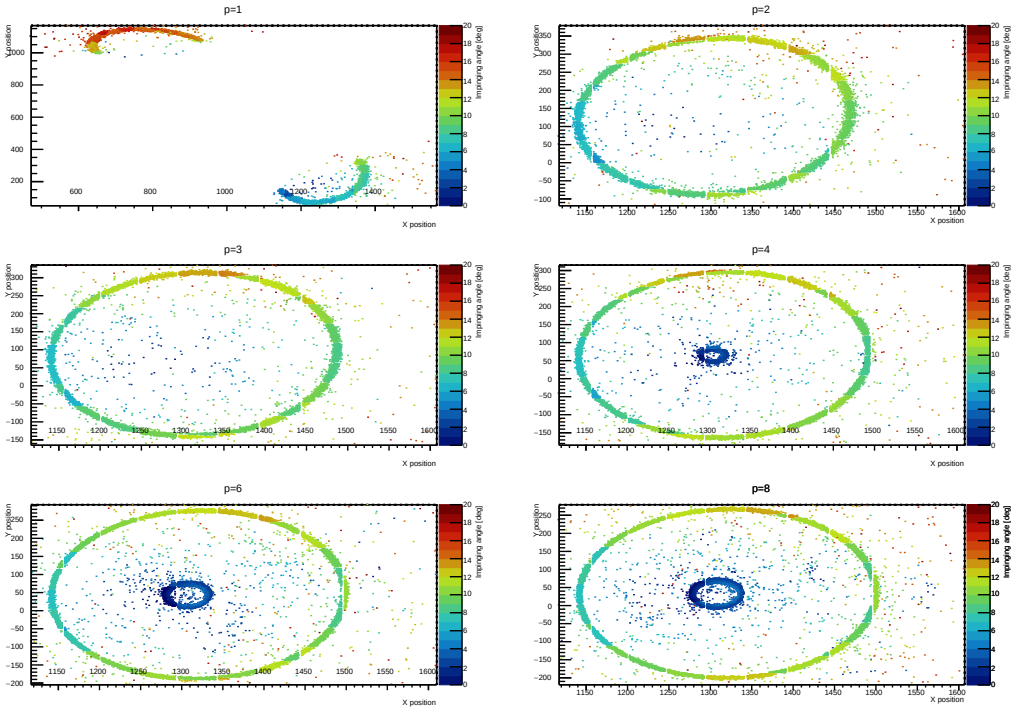

Figure 5.18: Dependency of the photon impinging angle as a function of momentum at fixed pseudorapidity = 2.0 is shown. Rings generated by the photons from both the gas and aerogel radiators are shown. 1000 pions were simulated.

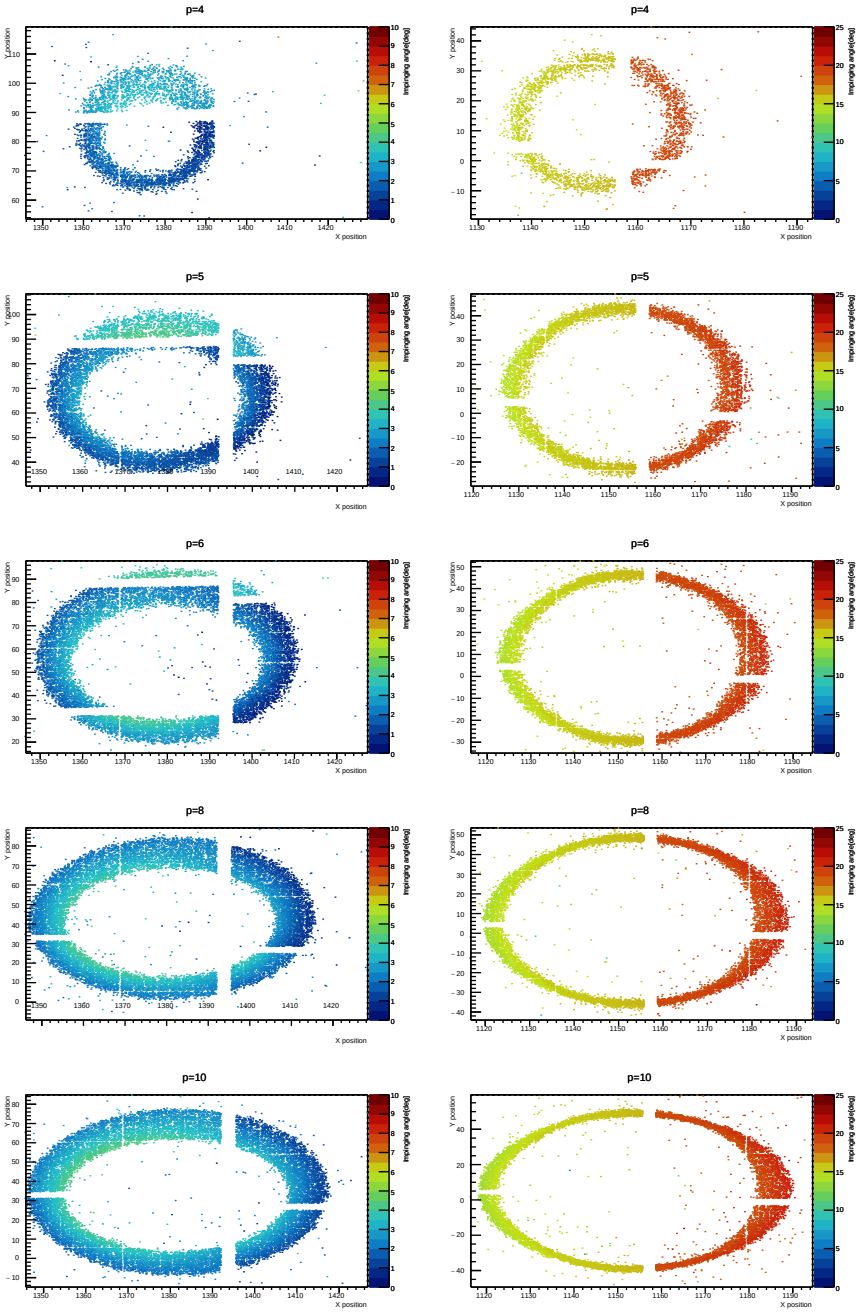

Figure 5.19: Dependency of the photon impinging angle as a function of momentum at two different values of pseudorapidity. Only the rings from the photons generated in the gas are shown. 1000 pions were simulated.

5.5 PID performance with added SiPM dark noise

The main challenge in using SiPMs for Cherenov imaging application is their intrinsic dark noise. The number of noise hits inside the ring region imposes challenge to particle identification by diluting the ring resolution. A simulation exercise has been made to study the effect of the added noise in terms of particle identification. To simulate this effect, white noise counts are added uniformly on the sensor surface before performing the reconstruction. The noise rate is defined for a single event and for each SiPM. In our exercise, on each SiPM, for each event, the added noise hits are $n \cdot t_w$, where n is the single SiPM noise rate and t_w the time window associate to an event. The maximum noise rate expected for the senors of the dRICH is 300kHz, while the time window is 1 ns. This results in a noise hit rate per event per SiPM of $3{\cdot}10^{-4}$. I have investigated how this affects the imaging performance.

In order to understand the feature of the noise hits and to have minimum bias from

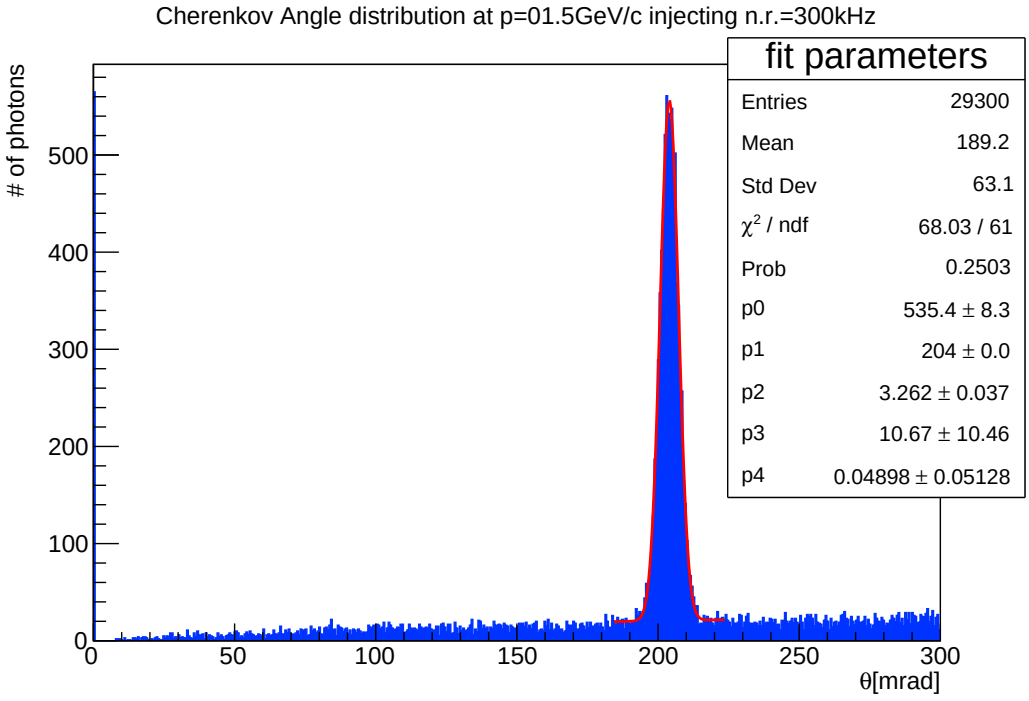

Figure 5.20: Cherenkov angle distribution for photons from aerogel for π of p=1.5GeV/c at $\eta = 2.0$ and noise rate of 300 kHz.

the reconstruction algorithm based on IRT technique we have used only one mirror

and sensor sector for our simulation studies. This ensures that the reconstruction algorithm picks up photons or noise hits that are only present in the sensor surface of interest. This consideration however does not bias any estimation, as in any running experiment hits that are present in non physical regions are always filtered out.

In Fig. 5.20, the reconstructed Cherenkov angle distribution of single detected photons for 1000 simulated single pion events with momentum 1.5 GeV/c is shown. We have injected 300 kHz of intrinsic noise. At this momentum the pions are under threshold for the gas radiator, we can in fact see that only one peak of aerogel photons is present. The background distribution grows linearly in the angular distribution because the noise has been injected uniformly.

In order to compute the noise contribution in the signal region, a combined fit with a Gaussian and a first order polynomial function has been used. The noise was computed as integral of the polynomial curve and the signal as the total counts subtracting the noise estimated bin by bin from the polynomial fit parameters. The integration limit is fixed within a window of 3 standard deviations of the Gaussian central value.

The computation of the noise under the signal peak allows us to estimate the purity we can achieve with this noise rate. We have studied the signal purity (defined as $signal/(signal + noise)$) as a function of momentum in both aerogel and gas radiators. We have used the new aerogel parameters for this study. In

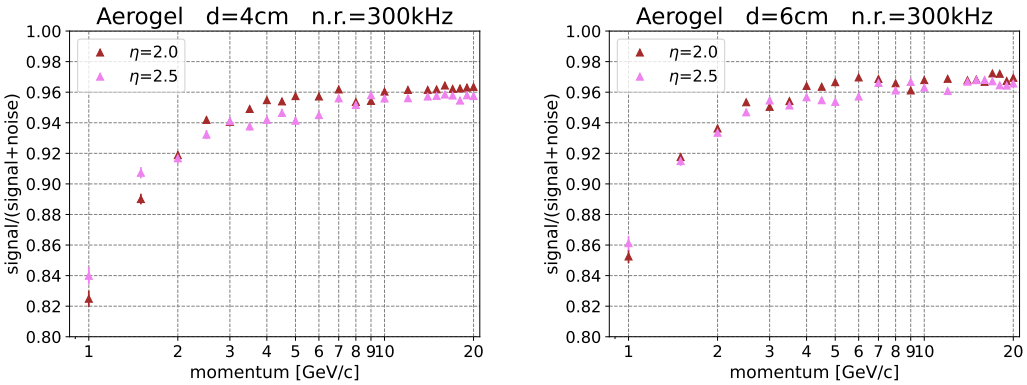

Figure 5.21: signal/(signal+noise) at different momentum for two different pseudorapidity-values with new aerogel of 4 cm (right) and 6 cm (left) thickness.

figure 5.21 the dependency of the signal purity as a function of momentum is plotted at two different fixed pseudorapdity-values. Two different values of the aerogel thicknesses have been studied. Due to the smaller number of photons generated with the 4 cm aerogel, the purity of the signal is lower in the whole momentum range. We have also studied the same effect in the gas radiator. The gas ring has

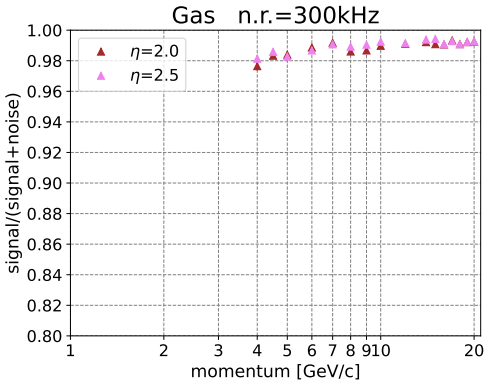

Figure 5.22: signal/(signal+noise) at different momentum for the gas radiator.

a smaller diameter, hence the amount of noise under the ring region is expected to be smaller than for the aerogel case. The amount of noise is expected to have a quadratic dependency from the Cherenkov angle. In our case, using the new aerogel, the number of photons at saturation for aerogel and gas is similar, therefore, we expect a quadratic dependence also for the purity. For the new aerogel the saturated ring angle is about 225 *mrad* and for the gas it is about 40 *mrad*. The average purity for saturated rings in the aerogel is ~ 0.96; therefore we expect the gas purity around $(\frac{(0.04)^2}{(0.225)^2} + 1) \cdot 0.96 \sim 0.99$ for the saturated rings. This intuitive calculation is in very good agreement with the outcome of the simulation as shown in Fig. 5.22. The effect of the noise on the ring resolution has been studied as a

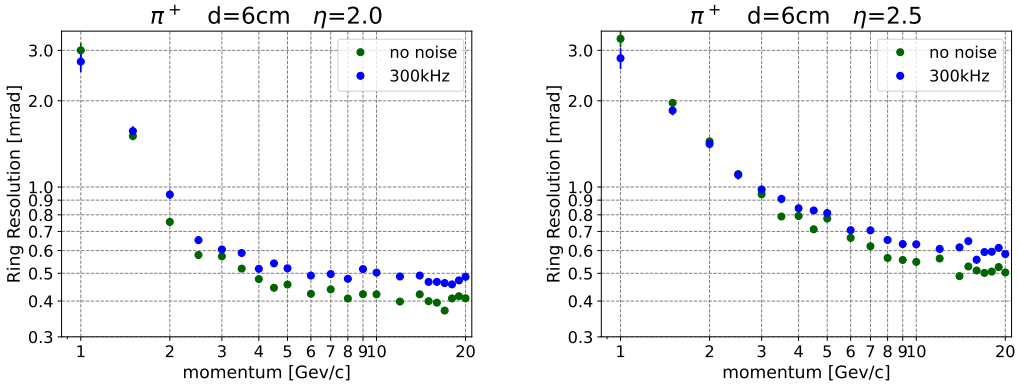

Figure 5.23: Ring resolution at two different pseudorapidity-values for simulated data without and with noise hits.

function of momentum. It is expected that the ring resolution gets worsen with added noise. From figure 5.23 we can notice that with injected noise, for aerogel,

the resolution degrades by $\sim 25\%$ for saturated rings. The PID performance of the new aerogel with added noise has been studied and presented in Fig. 5.24, where we can see that with added noise the 3σ separation limit for $\pi - \kappa$ reduces by $\sim 1\ GeV/c$ compared to the cases where no noise is injected. The reduction in performance is present in different pseudorapidity values. However, with 300 kHz injected noise, at $\eta = 2.0$ a 6 cm thick aerogel can provide 3σ $\pi - \kappa$ separation up to 18.5 GeV/c, whereas at similar condition for the aerogel with nominal thickness the performance is limited only up to 17 GeV/c.

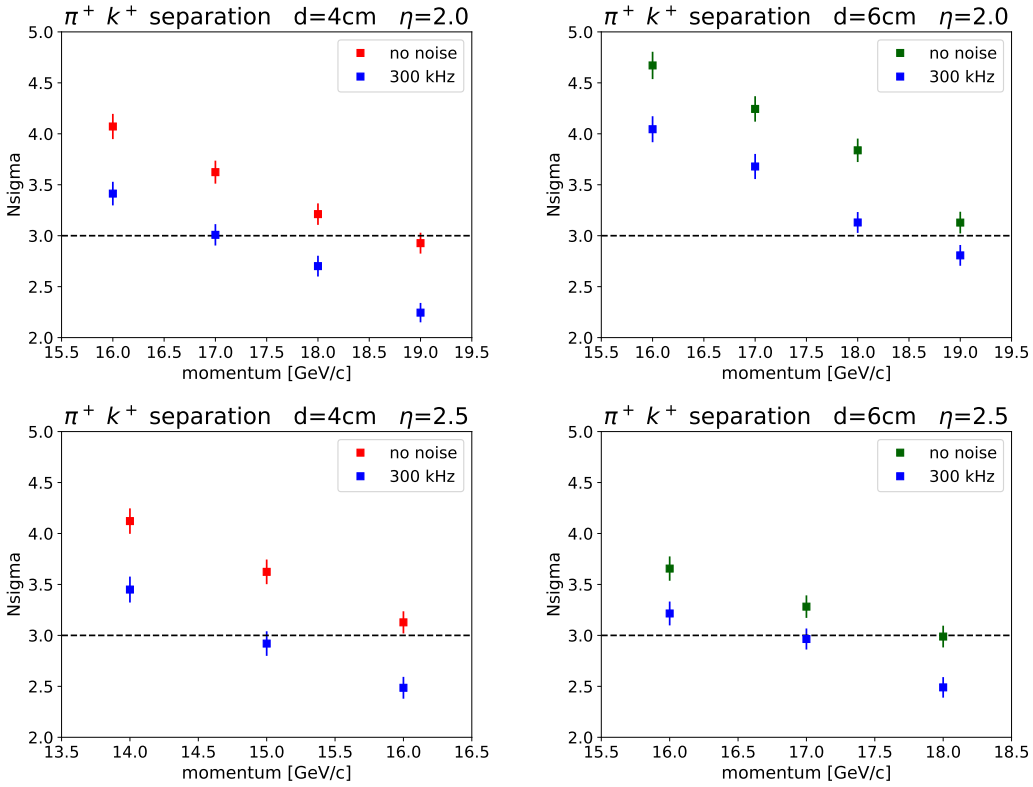

Figure 5.24: $\pi/|kappa$ separation with and without the injected noise at two different pseudorapity-values, new aerogel, 4 cm (left), 6 cm (right).

Chapter 6

Conclusions

The thesis aims to offer a complete panorama of the world of physics studies at high energy. In fact, it includes an overview of a physics domain, namely QCD, where key open questions are persistent and need further experimental investigation, of a novel large-size facility to progress in fundamental studies in physics, the EIC addressing ultimate QCD understanding, and of an up-to-date experiment in preparation to operate at EIC, namely the ePIC experiment. This panorama is made more complete by performing original studies contributing to the finalization of the design of the ePIC detector. These studies have been conducted by the student author of the thesis.

Three essential questions have been addressed within the original contribution presented in this thesis, which are of extreme important for the optimal design of the ePIC dRICH detector. The optimized choice of the aerogel characteristics and the performance limitations due to the sensor white noise are central ingredient for the PID performance of the dRICH detector. The estimation of the photon impinging angle on the sensor surface serves as a guide to the dRICH collaboration to measure in the laboratory the effective photon detection efficiency as a function of photon impinging angle. The probability that a photon is reflected back from the sensor surface and, therefore, not converted due to the large impinging angle, can result in an effective decrease in the number of detected photons. Hence, these effect deserves careful attention.

6.1 Studies with new aerogel parameters

Following the characterization of a new aerogel sample, a comparative study with respect to the aerogel already used in the experiment CLAS12 ("old aerogel") has been performed. It has been shown (Sec. 5.3) that the new aerogel performs better than the previously chosen type. The yield of detected photons using the

new aerogel type is on an average larger by a factor 1.3 both scanning versus pseudorapidity and versus momentum. The resolution in the Cherenkov angle measurement for the single photo electron is also better than for the old aerogel, thanks to the better optical parameters. A two fold improvement hence translates into setting higher momentum limit for 3-σ π-κ separation with the new aerogel radiator.

The number of photons can even be increased by employing thicker aerogel. A comparative study has been made with two different thicknesses. In our simulation, we have used a continuous block of aerogel, however in practice thicker aerogels will be realized by adding multiple layers. This imposes an irreducible surface effect, not taken into account in our exercise. In future, aerogel of multiple layers has to be simulated and studied. The studies of this thesis serves a reference for further investigation.

6.2 Studies with the impinging angle of the photons on sensor surface

The effective photon detection efficiencies as quoted in literature are usually measured with photon beams orthogonal to the sensor surface. These figures, hence, do not reflect the fact that Cherenkov photons impinging at a larger angle can be lost. The effects cannot be simulated becuase it depends on the unkonwn details of the SiPM covering window (material, shape). The exercise made in the thesis demonstrates that the photons produced in aerogel at maximum pseudorapidity can have a large impinging angle ($\sim 40^o$) when coming from off-sector mirrors (split rings). It is also noticed that for photon generated in the gas the impinging angle can be as large as 25^o for the high pseudorapidity region. The majority of the large momentum particles are scattered in the high pseudorapidity region. For these particles, the number of photons produced in gas is smaller due to the shorter path length, making the potential photon loss due to the impinging angle even more critical. Therefore, the effect on photon detection efficiency for photons impinging at large angles, as indicated by the simulation, has to measured and verified in the laboratory. In case of a strong dependency of the photon detection efficiency versus the photon impinging angle is observed in laboratory tests a re-optimization of the detector has to be considered.

6.3 Studies introducing the white noise from the sensor

Finally, we have performed exercises adding the white noise of the SiPM sensor. These studies are made for fully contained ring in one sector. The exercises have assumed different rates of added noise. The noise is integrated over a time window of 1 ns. The corresponding impact on the ring resolution and, consequently, on the π/κ separation level is obtained. The aerogel measurement is more affected than the gas one, because of the larger radius of the rings and the smaller number of detected Cherenkov photons. From the analysis it is evident that, with 300 kHz added noise, a value close to maximum noise expected in operation, one can reach 3σ π/κ separation up to 17 GeV with a 4 cm thick new aerogel. This is a O(1GeV) reduction in the performance as estimated without the added noise. The new aerogel demonstrated to perform better than the old aerogel even with added noise. The old aerogel could provide a 3σ π/κ separation without added white noise only up to 15 GeV for a fully contained aerogel ring. A summary of the noise performance for aerogel in provided in Table 6.1

Table 6.1: Comparison of π/κ separation performance with aerogel.

Noise (kHz)	Aerogel Thickness (cm)	Aerogel Type	3 σ limit π-K separation (GeV)
0	4	old	15
0	4	new	>18
300	4	new	17
0	6	new	19
300	6	new	18